Dynamical dark energy: Current constraints and forecasts

Amol Upadhye,[1] Mustapha Ishak,[2,3] and Paul J. Steinhardt[1]

[1]*Department of Physics, Princeton University, Princeton, New Jersey 08544, USA*
[2]*Department of Astrophysical Sciences, Princeton University, Princeton, New Jersey 08544, USA*
[3]*Department of Physics, The University of Texas at Dallas, Richardson, Texas 75083, USA*

(Received 11 March 2005; published 1 September 2005)

We consider how well the dark energy equation of state w as a function of redshift z will be measured using current and anticipated experiments. We use a procedure which takes fair account of the uncertainties in the functional dependence of w on z, as well as the parameter degeneracies, and avoids the use of strong prior constraints. We apply the procedure to current data from the Wilkinson Microwave Anisotropy Probe, Sloan Digital Sky Survey, and the supernova searches, and obtain results that are consistent with other analyses using different combinations of data sets. The effects of systematic experimental errors and variations in the analysis technique are discussed. Next, we use the same procedure to forecast the dark energy constraints achievable by the end of the decade, assuming 8 years of Wilkinson Microwave Anisotropy Probe data and realistic projections for ground-based measurements of supernovae and weak lensing. We find the 2σ constraints on the current value of w to be $\Delta w_0(2\sigma) = 0.20$, and on dw/dz (between $z = 0$ and $z = 1$) to be $\Delta w_1(2\sigma) = 0.37$. Finally, we compare these limits to other projections in the literature. Most show only a modest improvement; others show a more substantial improvement, but there are serious concerns about systematics. The remaining uncertainty still allows a significant span of competing dark energy models. Most likely, new kinds of measurements, or experiments more sophisticated than those currently planned, are needed to reveal the true nature of dark energy.

DOI: 10.1103/PhysRevD.72.063501 PACS numbers: 98.80.Es, 98.62.Sb, 98.65.Dx

I. INTRODUCTION

Several years ago, observations of supernovae of type Ia (SNe Ia) demonstrated that the expansion of the Universe is accelerating [1,2]. Associated with this acceleration is dark energy, a component with negative pressure, that makes up a significant fraction of the total energy density. Recent years have seen the supernova evidence for dark energy continue to mount [3–8]. Meanwhile, cosmic microwave background (CMB) data from the Wilkinson Microwave Anisotropy Probe (WMAP) project [9,10], in combination with information about either the Hubble constant [11] or the galaxy power spectrum [12,13], also requires the existence of dark energy. Cross-correlations between CMB anisotropies and matter power spectrum inhomogeneities provide evidence for a late-time integrated Sachs-Wolfe (ISW) effect [14–19]. This ISW effect indicates a recent change in the inhomogeneous gravitational potential, providing further evidence for dark energy.

One way to characterize the dark energy is to measure its equation of state, the ratio $w \equiv P/\rho$ of its pressure P and energy density ρ. The simplest model of the dark energy is a cosmological constant Λ, which has a constant $w = -1$. Quintessence models describe the dark energy as a dynamical scalar field with an equation of state $w \geq -1$, and, in general, w will not be constant in time [20–23]. Furthermore, models of extended quintessence or ''phantom energy'' even allow $w < -1$ [24].

Discovering whether or not the dark energy is a cosmological constant is the primary goal of the study of dark energy. If dark energy is shown not to be a cosmological constant, then the next important issues are whether or not $w < -1$, which can be theoretically problematic [25] (however, see [26–30] for an alternative viewpoint), and whether or not w is changing with time. While a quintessence with constant $w \approx -1$ is very difficult to distinguish quantitatively from a cosmological constant, the qualitative difference for fundamental physics is enormous, so it is critical that the maximum effort be made to reduce the uncertainty in $|w + 1|$ and its time derivative. Ultimately, the precise quantitative values of w and its time derivative are important for model building, but this is less crucial, at present, than the qualitative issue of whether the dark energy is dynamical or not. In order to address such questions about the nature of the dark energy, it is crucial that the equation of state and its time variation be determined observationally.

It has been known for some time that the cosmological probes used for studying the dark energy are plagued by numerous parameter degeneracies [31–37]. Because of these degeneracies, a large uncertainty in a cosmological parameter not directly related to the dark energy sector (e.g., the matter density) can lead to a large uncertainty in the dark energy equation of state. This sensitivity to other parameters means that one must incorporate the uncertainties in all parameters to obtain a realistic estimate of the uncertainties in the dark energy equation of state. In particular, one should avoid the use of strong priors on the form of $w(z)$, the values of other parameters, and independent information coming from other experiments. These

can lead to underestimates of the uncertainty in w by a very large factor. We will also discuss how standard likelihood marginalization can give a misleading impression of the uncertainty in w.

The analysis presented here employs a χ^2 minimization procedure in order to avoid possible problems with marginalization, and assumes only weak prior constraints. We compare our χ^2 minimization with the standard approach, the marginalization of a probability function computed using Monte Carlo Markov Chains. It is argued that our procedure gives a more conservative assessment of constraints in certain degenerate parameter spaces. In this sense, our procedure and the Markov Chain are complementary, as we will discuss.

We apply this χ^2 minimization analysis to the currently available data. The simultaneous determination of the dark energy equation of state and its redshift derivative is difficult without the combination of data from several cosmological probes. Thus we analyze the latest data from WMAP, SN Ia searches, and the Sloan Digital Sky Survey. Strong priors are avoided to prevent the underestimation of dark energy constraints. Although the data favor $w(0) < -1$ and $w'(0) > 0$, we are unable to rule out the cosmological constant conclusively. Furthermore, we find the constraints on $w(z)$ to depend strongly on the parametrization chosen for $w(z)$, as well as on the location of the best-fit model in parameter space, despite the fact that we have restricted our study to two-parameter equations of state. We also list possible biases in the cosmological probes, and discuss their effects on our results. Our conclusion that the cosmological constant is consistent with current data agrees with previous analyses, as we discuss in Sec. IV. This establishes the validity of our analytic methods, which we can then apply with confidence to projections of future measurements.

Since the cosmological constant is consistent with current data, it is useful to ask precisely how well dark energy may be constrained in the future using known cosmological probes. We address this question by applying our χ^2 minimization procedure to simulations of the data from these probes. Besides the CMB and SNe Ia, we simulate data from a probe of weak gravitational lensing (WL). In the future, WL is expected to be useful for constraining dark energy [38–51]. Most of these studies have demonstrated that WL breaks parameter degeneracies in the CMB analysis, and have shown the effectiveness of the combination of CMB and WL data in constraining dark energy.

Our study is the first to use a joint analysis of simulated CMB, SN Ia, and WL data, rather than imposing prior constraints as a ''replacement'' for one of these data sets. This is especially important for parameters such as $w(0)$ and $w'(0)$, which have strong degeneracies with other parameters. Since our goal is the study of $w(z)$ constraints, rather than general parameter constraints, we assume the cosmological model outside of the dark energy sector to be as simple as possible. Within this model, we are careful to avoid strong priors on the cosmological parameters. It is well understood that each of these cosmological probes has systematic uncertainties associated with it, and that significant progress needs to be made in order for each one to reach the level of precision necessary for constraining dark energy. Therefore, we attempt at every opportunity to strike a reasonable balance between optimism and realism.

The paper is organized as follows. Sec. II A discusses several parametrizations of the dark energy equation of state. Our choice of cosmological parameters, and the prior constraints imposed on them, are listed in Sec. II B. χ^2 minimization is compared with marginalization in Sec. II C. Section III A summarizes our analysis of current data, and Secs. III B, III C, and III D describe the simulation and analysis of future data. Finally, Sec. IV lists and interprets our findings, for our analysis of current data as well as our forecasts of future constraints, and Sec. V discusses our conclusions.

II. ANALYSIS METHODS

A. Dark energy parametrization

We have assumed that the dark energy may be parametrized using an equation of state $w(z) = P/\rho$, where P and ρ are the pressure and dark energy density, respectively, and $w(z)$ is an unknown function of redshift. We have also assumed that the dark energy sound speed is $c_s^2 = 1$. Without any theoretical guidance about the form of $w(z)$, the space of all possibilities is equivalent to an uncountably infinite set of cosmological parameters. The data depend on $w(z)$ only through a multiple integral relation [37], so we lack the large number of measurements of $w(z)$ that would be necessary for nonparametric inference [52]. Thus we must describe $w(z)$ using a small number of parameters in order to keep the analysis tractable. The danger is that there is no ''natural'' way to parametrize $w(z)$, so the choice of parametrizations is essentially arbitrary. Ideally, one would like to verify that any constraints obtained on $w(z)$ are parametrization-independent. However, the space of all possible parametrizations is infinite dimensional, so we are back to square one. The only feasible option is to test for parametrization independence by comparing constraints on a small number of ''reasonable-looking'' parametrizations.

To begin with, we assume that $w(z)$ is an analytic function, and that it can be approximated at $z \ll 1$ by the first few terms in its Taylor series about $z = 0$. All known probes are sensitive to an integral of some function of $w(z)$, rather than to $w(z)$ itself, so any ''bumps and wiggles'' in $w(z)$ are effectively smoothed out. It is reasonable to assume that this smoothed $w(z)$ can be approximated by a low-degree polynomial in z out to $z \lesssim 1$. From now on we proceed based on this assumption, with the caveat that the ''true'' equation of state can have added ''bumps and wiggles'' that disappear when smoothed. (Note, however,

that any large-scale kinks or sharp changes in the actual equation of state can be missed by such simple parametrizations. For an alternative approach, see, e.g., [53].)

The simplest parametrizations useful for describing dynamical dark energy have at least two parameters, one describing the equation of state $w(0)$ at $z = 0$ and the other parametrizing its redshift derivative $w'(0) \equiv \frac{dw}{dz}|_{z=0}$. A few parametrizations in the literature are

$$w(z) = w_0 + w'z \quad \text{(Simple parametrization)}, \tag{1}$$

$$w(z) = w_0 + (1 - a(z))w_a = w_0 + \frac{w_a z}{1+z} \tag{2}$$

(Refs. [54, 55]),

$$w(z) = w_0 + (1 - a(z))w_a + (1 - a(z))^2 w_b = w_0 + \frac{w_a z}{(1+z)} + \frac{w_b z^2}{(1+z)^2} \tag{3}$$

(Ref. [56]).

[Note that w_a in (3) differs by a factor of -1 from the definition introduced in [54]. We chose (3) in order to facilitate comparison with (2) and (4).] We are interested in the simplest two-parameter equations of state, and as we will see, (1) is of limited utility for studying high redshift data. This leaves only Eq. (2) out of the three parametrizations above. Since we would like to compare two "reasonable" two-parameter equations of state, we introduce a fourth parametrization,

$$w(z) = \begin{cases} w_0 + w_1 z & \text{if } z < 1, \\ w_0 + w_1 & \text{if } z \geq 1. \end{cases} \tag{4}$$

Dark energy constraints based on (2) and (4) may be compared in order to estimate the parametrization dependence of our results.

The high redshift limit of each parametrization becomes important when considering data from the CMB. Rather than providing information about $w(z)$ directly, the CMB data require only that the dark energy density be less than $\sim$10% of the critical density at the redshift of photon decoupling [55,56]. If $w(z) > 0$, the dark energy density will increase faster with redshift than the matter density, making the CMB constraint extremely difficult to satisfy. For the four dark energy parametrizations discussed above, the CMB effectively requires that $w(z) \leq 0$ at redshifts $z \gg 1$.

In each of the two- and three-parameter equations of state (1)–(4), this high redshift constraint prevents $w(z)$ from changing too rapidly at low redshifts. For fixed w_0, we see that: $w' \leq 0$ in (1); $w_1 \leq -w_0$ in (4); and $w_a \leq -w_0$ in (2). In particular, w_1 and w_a have the same upper bound. Note that these bounds arise purely from the choice of parametrizations for $w(z)$. There is no fundamental physical reason for assuming that an equation of state which becomes positive at redshift $z = 1$ will stay that way long enough to interfere with the physics at decoupling.

Figure 1 shows the upper bounds on the function $w(z)$ for each of the three parametrizations (1), (2), and (4), assuming $w_0 = -1$ in each case. Parametrization (1) disallows essentially all positive w'; we will not study it further. Meanwhile, (2) allows $w(z)$ to increase by $\bar{w}' = w(1) - w(0) = 0.5$ at low z, while (4) allows $w(z)$ to increase by $\bar{w}' = 1$. Some parameter combinations such as ($w_0 = -1$, $\bar{w}' = 0.6$) are acceptable in (4), but are simply not allowed in (2). That is, the two parametrizations cover different regions in the (w, z) plane. Of course, these parametrization-dependent effects of the high redshift $w(z)$ constraint will be important only if the dark energy is found to have $w(z) \sim 0$ at $z \gg 1$.

We choose to use parametrization (4) for most of the subsequent work, since it allows the widest range of $\bar{w}'$ values over the redshift range $0 \leq z \leq 1$, in which dw/dz is best constrained by the data. Outside of this range dw/dz is poorly constrained, so without loss of generality (4) makes the simple assumption $dw/dz = 0$. Equation (2) is also studied, and the results based on the two parametrizations are compared in order to estimate the parameterization dependence of our dark energy constraints. We describe the dynamics of the dark energy in terms of the ratio of the dark energy density to its value today, $\mathcal{Q}(z) \equiv \rho_{\rm de}(z)/\rho_{\rm de}(0)$. For parametrization (4), the fluid continuity equation can be used to show that

$$\mathcal{Q}(z) \equiv \begin{cases} (1+z)^{3(1+w_0-w_1)} e^{3w_1 z} & \text{if } z < 1, \\ (1+z)^{3(1+w_0+w_1)} e^{3w_1(1-2\ln 2)} & \text{if } z \geq 1. \end{cases} \tag{5}$$

[A corresponding expression for equation of state (2) can be found in [57,58].] Given our assumption of a flat universe, the Hubble parameter $H(z) \equiv \dot{a}/a$ evolves with redshift as follows:

$$H(z) = H_0 \sqrt{\Omega_m (1+z)^3 + (1 - \Omega_m)\mathcal{Q}(z)}. \tag{6}$$

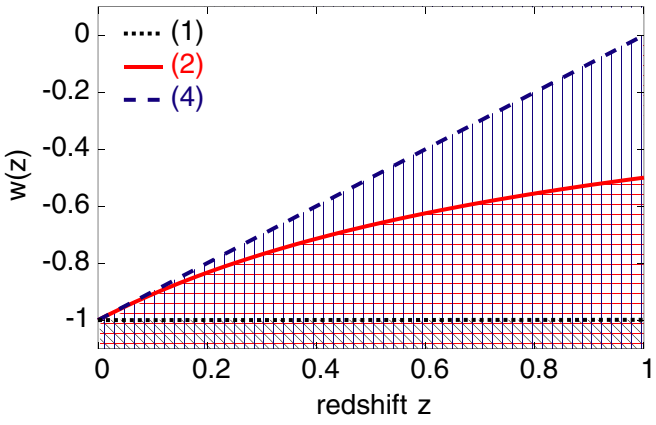

FIG. 1 (color online). Upper bounds on $w(z)$ for the three equations of state (1), (2), and (4). In all three cases, w_0 has been fixed at -1.

These results will be used in our discussions of the cosmological probes.

B. Cosmological parameters, degeneracies, and priors

Cosmology may be described using a large number of parameters corresponding to a wide range of possible effects. The approach taken by, e.g., [13] is to test for as many of these effects as possible; they describe cosmology in terms of 13 parameters. On the other hand, our aim is more specific. We wish to determine whether dynamical dark energy will be distinguishable from a cosmological constant by the end of the decade. If we can answer this question in the negative after considering only a subset of these 13 parameters, then the addition of more parameters will not change our conclusions. We find that even with a relatively limited set of parameters we will not be able to rule out dynamical dark energy. Thus, in the interests of simplicity and computational efficiency, we restrict ourselves to nine parameters.

Outside of the dark energy sector, we choose the simplest possible description of the Universe that is consistent with observations. The Universe is assumed to be flat, and we do not include tensor modes, massive neutrinos, or primordial isocurvature perturbations. Besides the dark energy parameters w_0 and w_1, our cosmological models are parametrized using $h \equiv H_0/(100 \text{ km sec}^{-1} \text{ Mpc}^{-1})$, where H_0 is the Hubble constant; $\omega_m \equiv \Omega_m h^2 = \rho_m h^2/\rho_{\text{crit}}$; $\omega_b \equiv \Omega_b h^2 = \rho_b h^2/\rho_{\text{crit}}$; τ, the optical depth to reionization; A, the normalization of the CMB power spectrum; n_s, the spectral index of the primordial power spectrum; and z_s, the characteristic weak lensing source redshift. (The WL source redshift was shown to be important in, e.g., [59–61].) Actually, [13] shows that n_s is not absolutely necessary, since the simple Harrison-Peebles-Zeldovich spectrum ($n_s = 1$) fits the data well. However, n_s is a well-motivated parameter whose degeneracies with the dark energy parameters could be important. Borrowing the terminology of [13], we call $(h, \omega_m, \omega_b, \tau, n_s, A)$ the "vanilla" parameters. Thus, our analysis adds to the simple vanilla model one parameter describing weak lensing sources, and two parameters describing the dark energy.

Our constraints based on this limited set of parameters will be optimistic, since including more parameters will tend to increase the uncertainties in w_0 and w_1. This is especially true when the parameters that we neglect are highly correlated with some of the parameters that we do consider. Reference [13] shows a strong degeneracy between the Hubble parameter h and the curvature Ω_K that could potentially affect our dark energy constraints. Also, [39] points out that neutrinos become important when using weak lensing in the nonlinear regime to study dark energy.

Even in our relatively simple parameter space, there exist several parameter degeneracies. A few examples are the angular diameter distance degeneracy [32,34–36] among h, Ω_m, Ω_b, and $w(z)$; the large-scale CMB degeneracy [31] among ω_m, τ, n_s, and $w(z)$; the small-scale CMB degeneracy [33] among τ, A, and n_s; and the supernova luminosity distance degeneracy [37] between Ω_m and $w(z)$. The presence of such parameter degeneracies means that several probes must be combined in order to obtain reliable constraints. Furthermore, combinations of known probes contain residual degeneracies, which we must deal with carefully in order to determine constraints on the dark energy.

In order to make a fair assessment of parameter degeneracies, it is necessary to avoid strong prior constraints on the cosmological parameters. Priors used here are listed in Table I. The above priors on w_0 and $w_0 + w_1$ are equivalent to the requirement that $w(z) \leq 0$ for all z.

The simulated data sets used here for constraint forecasts assumed a fiducial model $\{w_0 = -1,\ w_1 = 0,\ h = 0.7,\ \omega_m = 0.15,\ \omega_b = 0.023,\ \tau = 0.1,\ A = 0.8,\ n_s = 1,\ z_s = 1\}$. This roughly corresponds to the "vanilla lite" ΛCDM model of [13], with lensing sources assumed to be at characteristic redshift 1. Our chosen fiducial model implies $\Omega_m = 0.31$, $\Omega_b = 0.047$, and $\sigma_8 = 0.92$.

C. χ^2 minimization

In order to provide an accurate picture of the dark energy constraints in a degenerate parameter space, a χ^2 minimization procedure was used. Constraints on the dark energy parameters were determined using the 1σ and 2σ contours of the χ^2 function in the (w_0, w_1) plane. At any given point (w_0, w_1), $\chi^2(w_0, w_1)$ was computed by minimizing over all other cosmological parameters.

χ^2 minimization handles certain types of degeneracies more carefully than marginalization, the procedure most commonly used to obtain cosmological constraints, meaning that the two methods are complementary. Marginalization favors models that fit well over "large" regions of parameter space. Given two cosmological models with the same low χ^2, marginalization will give extra weight to the model that sits in a large region of low-χ^2

TABLE I. Summary of the prior constraints assumed for the χ^2 minimization analysis.

Parameter	Lower bound	Upper bound
h	0.4	1.1
ω_b	0.003	ω_m
ω_m	ω_b	1
Ω_m	0	1
Ω_K	0	0
τ	0	1
A	0.5	1.5
n_s	0.5	1.5
z_s	0	1.5
w_0	...	0
$w_0 + w_1$	...	0

models. Meanwhile, χ^2 minimization will pick the best model while completely ignoring its surroundings. These differences are illustrated in Fig. 2, based on a sample χ^2 function of two arbitrary parameters x and y. The 1σ contour of $\chi^2(x, y)$ is shown in Fig. 2 (top). Note that the contour has a small slope at low x, but is nearly parallel to the y axis at high x.

If we are interested only in constraints on x, then we can either minimize or marginalize over y. Figure 2 (middle) sketches the probability functions obtained using the two different methods. Consider the two models A and B, at x_A and x_B, respectively, whose y values are chosen to minimize $\chi^2(x, y)$ at the corresponding x values. Minimization takes the viewpoint that, since $\chi^2_A \approx \chi^2_B$, the x values x_A and x_B are approximately equally probable. On the other hand, marginalization assigns a much greater probability to x_B, since there are many more low-χ^2 models at x_B than at x_A. Thus the χ^2-minimized probability distribution looks like a broad plateau, while the marginalized probability looks like a sharp peak with a "shoulder." The bounds on x obtained from these two methods, as shown in Fig. 2 (bottom), are quite different. Note that this discussion is not just academic. The CMB 95% probability contour in the $(h, \Omega_{\rm tot})$ plane, shown in Fig. 7 of [13], is qualitatively very similar to the contour shown here in Fig. 2 (top).

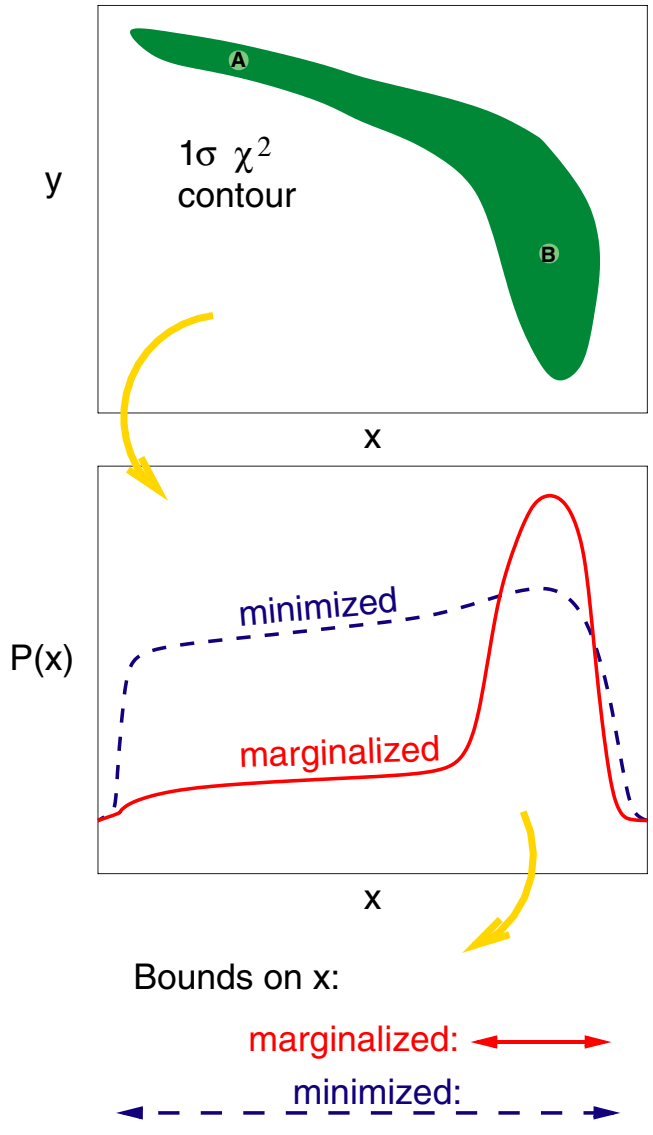

FIG. 2 (color online). Comparison of minimization and marginalization in a (hypothetical) degenerate parameter space. Two models, A and B, are labeled. Top: Sample 1σ contour of $\chi^2(x, y)$ in a degenerate parameter space. Middle: Probability functions based on minimization and marginalization. Bottom: Constraints on x based on minimized and marginalized probability functions.

The parameter bounds derived from marginalization have excluded models such as A, which are within the 1σ χ^2 contour. A procedure that excludes such models can be problematic for two reasons. First of all, it is not clear that low-χ^2 models such as A really should be ignored; it is prudent, at least, to know of the existence of such a model. Ignoring such points can lead to an underestimate of the size of a degenerate region, so they should be considered in a proper treatment of parameter degeneracies.

Second, the notion of size in parameter space depends on the prior constraints chosen. For a parameter vector $\mathbf{p}$ of N parameters, the *a posteriori* probability marginalized over all but m of the parameters is given by

$$\mathcal{P}(p^0, \ldots, p^{m-1}) = \int dp^m \ldots dp^{N-1} \mathcal{L}(\mathbf{p}) \mathcal{P}_{\rm prior}(\mathbf{p}). \quad (7)$$

It is customary to reduce this dependence on priors by choosing uniform priors, with $\mathcal{P}_{\rm prior}(\mathbf{p})$ constant on a subset of parameter space and zero elsewhere. However, the concept of uniform priors is itself parametrization dependent. Choosing priors that are uniform in a different set of parameters $\mathbf{q}$ is equivalent to letting $\mathcal{P}_{\rm prior}(\mathbf{p})$ equal the Jacobian determinant of the transformation from $\mathbf{p}$ to $\mathbf{q}$.

On the other hand, marginalization has several advantages of its own. First of all, one can always come up with a $\chi^2(x, y)$ function which is handled correctly by marginalization, but for which minimization implies artificially tight constraints. Also, marginalization naturally defines a probability in parameter space. An analysis based on marginalization is capable of providing probability contours, which may be more useful than χ^2 contours. For a non-Gaussian likelihood function, there is no simple way to relate contours of $\chi^2(\mathbf{p})$ to a given probability contour without marginalization. Meanwhile, it may be the case that a natural set of parameters exists for describing a theory, such as h, Ω_m, and Ω_b in general relativistic cosmology. The existence of natural parameters makes it easier to choose a reasonable prior probability distribution $\mathcal{P}_{\rm prior}$, since one no longer needs to worry about reparametrization changing the form of $\mathcal{P}_{\rm prior}$. Constraints de-

rived from a marginalization over such parameters, assuming weak and uniform priors, can be quite convincing.

We take the point of view that any final constraints on w_0 and w_1 should be independent of the analysis method used. If a claim made using one of the two methods does not hold up to scrutiny by the other method, then the issue is too close to call. For example, we do not believe that model A in Fig. 2 is ruled out, even though it is excluded by marginalization over y. In this sense, χ^2 minimization and marginalization are complementary analysis techniques that are useful for handling different types of parameter degeneracies in a non-Gaussian likelihood function. We have chosen to use χ^2 minimization, partly because we are concerned about degenerate regions such as in Fig. 2 (top), and partly because it is not clear which parameters should be used to describe dark energy, reionization (τ or $z_{\rm reion}$), and the power spectrum amplitude (A or σ_8).

For completeness, we discuss a few computational issues here. Minimizations were performed using the Amoeba routine of [62], although the Powell routine from that reference was found to give very similar results. The computation was sped up by generating CMB power spectra for 100 different n_s values at once, and interpolating to find χ^2 for intermediate n_s values. This gave us information about χ^2 over our entire range of n_s values with just one call to CMBFAST. (Interpolation-related errors in χ^2 were found to be negligible.) Also, we minimized separately over the three parameters A, n_s, and z_s, since a variation in one of these parameters did not require the recomputation of CMB power spectra. This minimization over A, n_s, and z_s was nested within the minimization over h, ω_m, ω_b, and τ.

III. COSMOLOGICAL PROBES

A. Current data

Since our analyses of current data follow standard procedures, we will discuss them only briefly.

Supernovae of type Ia.—SNe Ia are standardizable candles [63–66], with magnitude $m(z) = 5\log_{10}(D_L(z)) + \mathcal{M}$ (see, e.g., [67]). The dimensionless luminosity distance $D_L(z) = (1+z)H_0 \int_0^z dz'/H(z')$ depends on Ω_m and the dark energy parameters through $H(z)$, given in (6). Our analysis minimizes χ^2 with respect to the magnitude parameter $\mathcal{M}$, which is dependent on H_0 and the SN Ia absolute magnitude.

Cosmic microwave background.—For the dynamical models of dark energy considered here, power spectra were computed with a modified version of CMBFAST 4.1 [68,69]. Our analysis of the data used our own implementation of the CMB χ^2 function described in [70]. Noise parameters and constants describing the WMAP parametrization of the Fisher matrices were taken from [71,72].

Galaxy power spectrum.—Our analysis of Sloan Digital Sky Survey (SDSS) data used the galaxy power spectrum [12] and the likelihood code of [13], made publicly available at [73]. Given a cosmological model, the corresponding matter power spectrum was computed using CMBFAST. The normalization of the power spectrum was treated as a nuisance parameter; χ^2 was minimized with respect to it. An accurate formula for the matter power spectrum in the nonlinear regime, for dynamical dark energy cosmologies, is not currently available. Furthermore, galaxy biasing in the nonlinear regime is even less well understood. Therefore, the SDSS data analysis presented here only used measurements for $k \leq 0.15h/\mathrm{Mpc}$ [13].

B. SN Ia simulation

1. Supernova simulation strategies

Monte Carlo techniques were used to simulate the magnitudes and redshifts of type Ia supernovae, from previous, current, and future supernova surveys, that would be available for analysis by the end of the decade. Rather than mixing real and simulated data, it was decided to simulate all of the surveys from scratch, so that all data used would be drawn from the same (known) fiducial model. In order

TABLE II. Numbers and redshift distributions of simulated type Ia supernovae.

SN Ia data set	Number of SNe Ia	Redshift distribution
Current (low z) [5,7]	83	uniform, $0.01 < z < 0.1$
Current (mid z) [5–7]	117	Gaussian, $z_{\rm mean} = 0.55$, $\sigma_z = 0.25$
Current (high z) [8]	16	Gaussian, $z_{\rm mean} = 1.0$, $\sigma_z = 0.4$
Carnegie (low z) [74]	94	uniform, $0.01 < z < 0.07$
Carnegie (high z) [74]	90	Gaussian, $z_{\rm mean} = 0.4$, $\sigma_z = 0.2$
DE Camera [75]	570	Gaussian, $z_{\rm mean} = 0.55$, $\sigma_z = 0.25$
ESSENCE [76–78]	150	uniform, $0.15 < z < 0.75$
PANS [79,80]	80	Gaussian, $z_{\rm mean} = 1.0$, $\sigma_z = 0.4$
SDSS [81]	100	uniform, $0.05 < z < 0.15$
SNfactory [82]	225	uniform, $0.01 < z < 0.1$
Supernova Legacy Survey [83–86]	525	Gaussian, $z_{\rm mean} = 0.6$, $\sigma_z = 0.3$
Total	2050	

to conduct a realistic simulation of future supernova surveys, we studied the available literature, including analyses of current data as well as plans for future surveys. For each SN Ia survey we estimated the expected number of supernovae to be observed and modeled a SN Ia redshift distribution. The final simulated SN Ia data set included 2050 supernovae ranging in redshift from 0.01 to 2.0, as summarized in Table II. Our simulation was based upon the following assumptions, which we justified by reference to data whenever possible.

(i) Twenty-five percent of the SNe Ia found by each survey were assumed to be unusable for cosmological analysis. This is based on the fact that 23% of the SNe Ia in the Tonry/Barris data set [5,7] did not survive their cuts on very low redshifts ($z < 0.01$) and galactic host extinctions.

(ii) Two-thirds of all low redshift SNe (of all types) were assumed to be of type Ia, based on the supernovae reported in [82].

(iii) Redshift distributions were assumed to be uniform for low redshifts. Since $m(z)$ at low redshifts is independent of cosmological parameters other than $\mathcal{M}$, the details of the redshift distribution for $z \lesssim 0.1$ should be unimportant for parameter constraints.

(iv) Redshift distributions were assumed to be Gaussian [$P(z) \propto \exp(-(z - z_{\rm mean})^2/(2\sigma_z^2))$] for higher redshift surveys, unless otherwise specified in the literature.

(v) Current data reported in [5–8] were simulated by dividing them into three ''surveys:''
low z, Tonry/Barris SNe Ia with $z < 0.1$;
mid z, SNe Ia from [5–7] with $z > 0.1$;
high z, Hubble Space Telescope Great Observatories Origins Deep Survey SNe Ia [8].
This was done because the current data come from a collection of previous surveys over a wide range of redshifts, and are poorly approximated by uniform or Gaussian distributions.

(vi) Forty percent of the expected Dark Energy Camera [75] data were assumed to be available, bringing the total number of supernovae to just over 2000. Even under optimistic assumptions about systematic uncertainties, we do not expect an increase in the number of SNe beyond this point to improve constraints on dark energy [87].

2. Magnitude uncertainties

A well-studied SN Ia sample, with accurate spectroscopic measurements of the supernova host galaxy redshifts, can have an intrinsic magnitude uncertainty for each supernova as low as $\sigma_m^{(\rm int)} = 0.15$ [75,83]. If less accurate host redshift information is available, the magnitude uncertainty suffers; [75] estimates an uncertainty of $\sigma_m^{(\rm int)} \sim 0.25$ when only photometric redshift information is available for the host galaxies. Meanwhile, the average magnitude uncertainty in the Tonry/Barris sample, for SNe Ia in the redshift range $0.1 < z < 0.8$, is $\sigma_m^{(\rm int)} = 0.3$. Since the final data set will be a combination of many supernovae with varying amounts of redshift information, the approach adopted here is to assume a magnitude uncertainty of $\sigma_m^{(\rm int)} = 0.2$ for supernovae in the intermediate redshift range $0.1 < z < 0.8$.

Judging from the supernovae tabulated in [5,7], the low redshift supernovae tend to have smaller magnitude uncertainties than average. The mean magnitude uncertainty is 0.18 for the $z < 0.1$ SNe Ia, compared to 0.25 for the full Tonry/Barris sample. Thus, for the purposes of this simulation, it is assumed that the magnitude uncertainty for each low redshift ($z < 0.1$) supernova is the minimum value, $\sigma_m^{(\rm int)} = 0.15$.

Meanwhile, supernovae at redshifts greater than about 0.8–1.0 become increasingly difficult to observe from the ground, and the spectroscopic analyses of such SNe Ia become very time-consuming [83,88]. In the Tonry/Barris sample, the magnitude uncertainty rises from a mean of 0.3 in the redshift range $0.1 < z < 0.8$ to 0.35 in the range $z > 0.8$. Based on this, it was decided to assume an intrinsic magnitude uncertainty of $\sigma_m^{(\rm int)} = 0.25$ for supernovae with $z > 0.8$.

It is necessary to include an extra uncertainty to account for the nonzero peculiar velocities of actual supernovae. Following [5], it was assumed here that the peculiar velocity uncertainty of each supernova was $\sigma_v = 500$ km/ sec. The fractional uncertainty in the luminosity distance due the peculiar velocity uncertainty was taken to equal the fractional uncertainty $(\sigma_v/c)/z$ in redshift. The resulting contribution to the magnitude uncertainty is $\sigma_m^{(\rm pec)} = 5\sigma_v/(cz\ln(10))$, where c is the speed of light.

Finally, following [87], we assumed a systematic uncertainty that prevents constraints on the apparent magnitude $m(z)$ from becoming arbitrarily tight. In the absence of such a systematic effect, the magnitude uncertainty in a bin containing $N_{\rm bin}$ supernovae will be $\sigma_m/\sqrt{(N_{\rm bin})}$, which approaches zero with increasing $N_{\rm bin}$. To this we add $\delta m = 0.04$ in quadrature, which imposes a floor δm on the uncertainty in each bin. We choose the bin size $\Delta z = 0.1$; this acts as a ''correlation length'' for the systematic. For a single supernova in a bin containing $N_{\rm bin}$ supernovae, this systematic implies an effective magnitude uncertainty

$$\sigma_m^{(\rm eff)} = \sqrt{(\sigma_m^{(\rm int)})^2 + (\sigma_m^{(\rm pec)})^2 + N_{\rm bin}\delta m^2}, \qquad (8)$$

which increases with increasing $N_{\rm bin}$.

3. The complete SNe Monte-Carlo data set

Monte Carlo supernova ''data'' points were generated using the redshift distributions and magnitude uncertainties specified above. For each supernova from each simu-

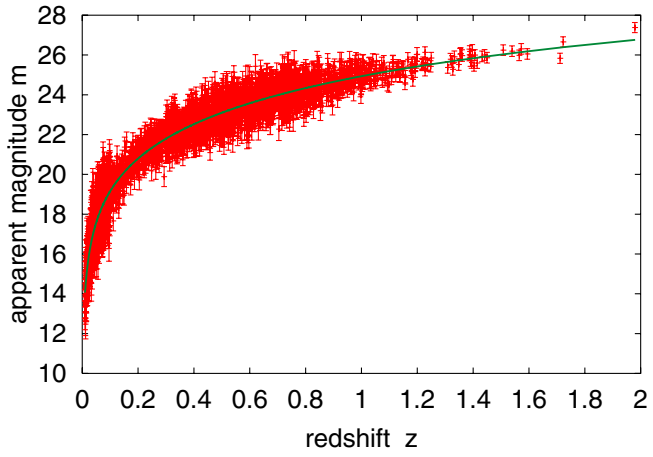

FIG. 3 (color online). The simulated SN Ia data set. The points with error bars are the simulated supernovae, while the solid line is the fiducial model.

lated experiment, the appropriate redshift distribution was used for the random generation of a redshift z. Next, the apparent magnitude $m^{(\mathrm{fid})}(z)$ expected for a supernova at redshift z was computed for the fiducial model used here: $\Omega_m = 0.31$, $w_0 = -1$, $w_1 = 0$. The magnitude uncertainty $\sigma_m^{(\mathrm{eff})}(z)$ for that supernova was computed as described in the previous subsection. Finally, the simulated apparent magnitude $m^{(\mathrm{MC})}$ was computed by adding to $m^{(\mathrm{fid})}(z)$ a random number chosen from a Gaussian distribution, with mean zero and standard deviation $\sigma_m^{(\mathrm{eff})}$. These Monte-Carlo simulated magnitudes $m^{(\mathrm{MC})}$, along with their corresponding redshifts and magnitude uncertainties, formed the simulated data set used here.

Table II lists the numbers and redshift distributions of the supernovae simulated, and Fig. 3 plots the magnitude-redshift relation of the simulated data. Note that, since the major supernova surveys planned over the next several years are ground based, the simulated data set contains very few supernovae with redshift greater than about 1.2.

C. CMB simulation

1. CMB covariance matrix

In the following discussion, we use the convention of [89] that $C_l = l(l+1)C_l/(2\pi)$ for any power spectrum C_l. We computed variances in the C_ls using the expressions given in [70,72] for the diagonal components of the covariance matrices. The noise parameters $\mathcal{N}_l^{TT}$ and $\mathcal{N}_l^{EE}$ were defined to be 1/8 of those used by WMAP, in order to simulate the effects of using eight years of WMAP data. WMAP noise parameters were taken from their data tables, which were described in [71,72], and provided along with the WMAP likelihood code described in [70]. The effective noise parameter $\mathcal{N}_l^{TT,(\mathrm{eff})}$, as a fraction of the original noise parameter $\mathcal{N}_l^{TT}$, and the effective sky fraction $f_{\mathrm{sky}}^{(\mathrm{eff})}(l)$ were defined as in [70]. The final expression for the uncertainties in the C_l^{TT}s was therefore taken to be

$$\sqrt{\mathrm{Var}(TT)} = \frac{C_l^{TT,(\mathrm{theory})} + \mathcal{N}_l^{TT,(\mathrm{eff})}}{\sqrt{(l+\frac{1}{2})f_{\mathrm{sky}}^{(\mathrm{eff})2}}}. \tag{9}$$

Note that (9) is a more conservative expression for the variance than that given by [89], since there is an "extra" factor of f_{sky} in the denominator of Var(TT). The information "lost" by dividing Var(TT) by f_{sky} is actually stored in the off-diagonal components of the covariance matrix (which we ignored), because nearby C_ls are anti-correlated [70]. However, we found that this extra f_{sky} had only a negligible effect on our forecast constraints.

We used a similar form for the uncertainty in the E-mode polarization power spectrum C_l^{EE}. Since WMAP did not include the C_l^{EE}s in the likelihood analysis of their first-year data, effective corrections to the noise and sky fraction were not computed. We used $f_{\mathrm{sky}} = 0.85$ and $\mathcal{N}_l^{EE,(\mathrm{eff})} = \mathcal{N}_l^{EE}$.

$$\sqrt{\mathrm{Var}(EE)} = \frac{C_l^{EE,(\mathrm{theory})} + \mathcal{N}_l^{EE}}{\sqrt{(l+\frac{1}{2})f_{\mathrm{sky}}^2}}. \tag{10}$$

Finally, uncertainties for the cross-power spectrum C_l^{TE} were taken from Eq. (10) in [72], using $f_{\mathrm{sky}} = 0.85$ and $f_{\mathrm{sky}}^{TE,\mathrm{eff}} = \frac{f_{\mathrm{sky}}}{1.14}$ as described in that reference.

$$\mathrm{Var}\,(TE) = \frac{(C_l^{TT} + \mathcal{N}_l^{TT})(C_l^{EE} + \mathcal{N}_l^{EE}) + (C_l^{TE})^2}{(2l+1)f_{\mathrm{sky}}f_{\mathrm{sky}}^{TE,\mathrm{eff}}}. \tag{11}$$

Even in the absence of a sky cut, correlations exist among the three power spectra C_l^{TT}, C_l^{TE}, and C_l^{EE} for each l [33]. As above, we keep the extra factor of f_{sky} in the denominators of the expressions given in that reference. For a given multipole l, the covariance matrix $\mathbf{C}_{XY}$, where $X, Y = TT$, TE, or EE, is given by

$$\mathbf{C}_{XX}^{(l)} = \mathrm{Var}(X), \tag{12}$$

$$\mathbf{C}_{TT,TE}^{(l)} = \frac{(C_l^{TT} + \mathcal{N}_l^{TT})C_l^{TE}}{(l+\frac{1}{2})f_{\mathrm{sky}}^2}, \tag{13}$$

$$\mathbf{C}_{TT,EE}^{(l)} = \frac{(C_l^{TE})^2}{(l+\frac{1}{2})f_{\mathrm{sky}}^2}, \tag{14}$$

$$\mathbf{C}_{TE,EE}^{(l)} = \frac{(C_l^{EE} + \mathcal{N}_l^{EE})C_l^{TE}}{(l+\frac{1}{2})f_{\mathrm{sky}}^2}. \tag{15}$$

Large-l correlations are also expected to exist between the CMB power spectra and large-scale structure, due to the Sunyaev-Zeldovich effect [90,91] and the gravitational lensing of the CMB [92,93]. However, these effects are too small to detect today [94–96]. The analysis presented here

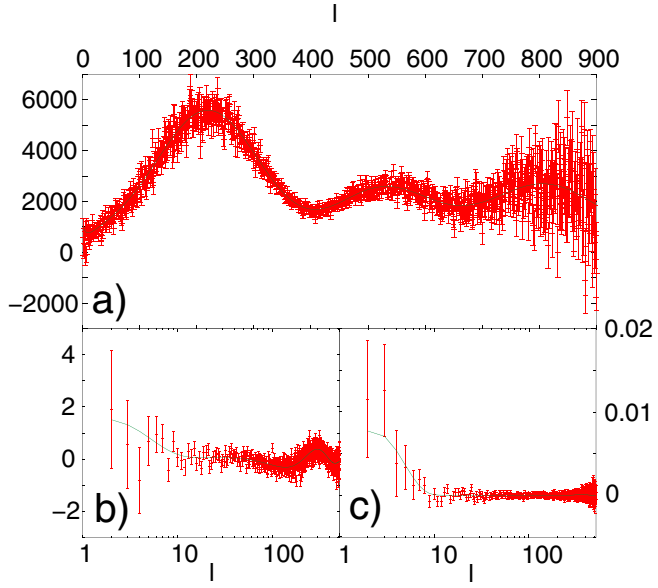

FIG. 4 (color online). WMAP-8 simulated power spectra $l(l+1)C_l/(2\pi)$: (a) TT, (b) TE, and (c) EE spectra, in units of μK^2. The points with error bars are the simulated data, while the solid lines are the fiducial models.

neglected such correlations. In particular, we assumed the CMB χ^2 function to be independent of the redshifts z_s of weak lensing sources.

2. Simulation

A set of simulated TT, TE, and EE CMB power spectra was generated by means of a Monte-Carlo simulation. For the purposes of this simulation, it was assumed that the WMAP project [9] would be extended to eight years. Data from the Planck mission, as described in [97,98], were not simulated for this work; the analysis of Planck data will be complicated by nonlinear effects such as the gravitational lensing of the power spectra.

The WMAP-8 data set described here contained eight years of simulated WMAP data. We simulated TT data up to a maximum multipole of $l^T_{\rm max} = 900$, and TE and EE data up to $l^E_{\rm max} = 512$, taking care to include the appropriate correlations among the three power spectra at each l. As detailed above, we divided by eight the tabulated WMAP noise parameters from one year of data. Non-Gaussianities in the distributions of observed C_l values about the underlying model have been ignored; see [89] for a discussion of such effects. The simulated TT, TE, and EE power spectra are shown in Fig. 4.

D. Weak lensing simulation

1. Convergence power spectrum

In the Limber approximation, the convergence power spectrum is given by [99–101]

$$P^\kappa_l = \frac{9}{4} H_0^4 \Omega_m^2 \int_0^{\chi_H} \frac{g^2(\chi)}{a^2(\chi)} P_{\rm 3D}\left(\frac{l}{\sin_K(\chi)}, \chi\right) d\chi, \qquad (16)$$

where $P_{\rm 3D}$ is the 3D nonlinear power spectrum of the matter density fluctuation, δ; $a(\chi)$ is the scale factor; and $\sin_K\chi = K^{-1/2}\sin(K^{1/2}\chi)$ is the comoving angular diameter distance to χ (for the spatially flat universe used in this analysis, this reduces to χ). The weighting function $g(\chi)$ is the source-averaged distance ratio given by $g(\chi) = \int_\chi^{\chi_H} d\chi' n(\chi')\sin_K(\chi'-\chi)/\sin_K(\chi')$, where $n(\chi(z))$ is the source redshift distribution normalized by $\int dz n(z) = 1$. We assume that all the sources are at a characteristic redshift z_s, so this reduces to $g(\chi) = \sin_K(\chi_s - \chi)/\sin_K(\chi_s)$. For weak lensing calculations, we use the standard BBKS transfer function [102], and the analytic approximation of Ref. [103] for the growth factor. We use the mapping procedure HALOFIT [104] to calculate the nonlinear power spectrum.

2. The weak lensing χ^2 function

For the weak lensing spectrum, the uncertainty is given by [99,101]

$$\delta P^\kappa_l = \sqrt{\frac{2}{(2l+1) f_{\rm sky}}}\left(P^\kappa_l + \frac{\langle \gamma^2_{\rm int}\rangle}{\bar{n}}\right), \qquad (17)$$

where $f_{\rm sky} = \Theta^2\pi/129\,600$ is the fraction of the sky covered by a survey of dimension Θ in degrees, and $\langle\gamma^2_{\rm int}\rangle^{1/2} \approx 0.4$ is the intrinsic ellipticity of galaxies. We consider a reference survey with $f_{\rm sky} = 0.7$, in the same range as the Pan-STARRS survey [105]. We used an average galaxy number density of $\bar{n} \approx 6.6\times10^8{\rm sr}^{-1}$. χ^2 was computed between multipoles $l_{\rm min}$ and $l_{\rm max}$. For $l_{\rm min}$, we took the fundamental mode approximation: $l_{\rm min} \approx 360\ {\rm deg}/\Theta = \sqrt{\pi/{\rm f_{sky}}}$, i.e. we considered only lensing modes for which at least one wavelength can fit inside the survey area. We used $l_{\rm max} = 3000$, since on smaller scales the nonlinear approximation HALOFIT to the nonlinear power spectrum may not be valid.

3. Simulation

The procedure described above was used to generate fiducial convergence power spectra $P^{\kappa,({\rm fid})}_l$. We used the cosmological parameter fiducial values of Sec. II A. We then calculated the uncertainties on the convergence power spectra using Eq. (17). The Monte-Carlo simulated convergence power spectra are generated using $P^{\kappa,{\rm MC}}_l = P^{\kappa,({\rm fid})}_l + r\delta P^\kappa_l$, where r is randomly chosen from a Gaussian distribution of standard deviation 1 [62]. The simulated convergence power spectrum for the reference survey and the fiducial model are shown in Fig. 5.

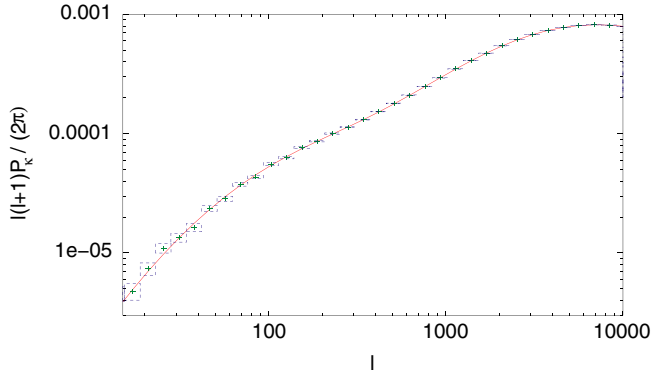

FIG. 5 (color online). Monte Carlo simulated convergence power spectrum. The points with error boxes are the simulated data for a survey with $f_{\rm sky} = 0.7$, $\bar{n} \approx 6.6 \times 10^8$ sr^{-1}, and $\langle \gamma^2_{\rm int} \rangle^{1/2} \approx 0.4$, while the solid line is the fiducial model.

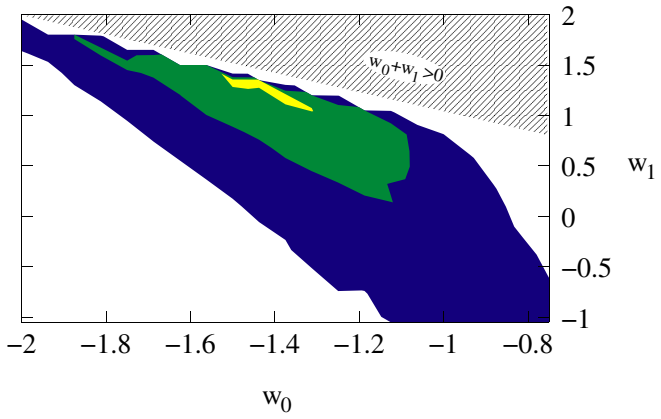

FIG. 6 (color online). Current constraints on dynamical dark energy parametrized by (4), using first-year WMAP data, the SNe Ia "gold set" from [8], and the current SDSS data. The 1σ, 2σ, and 3σ contours are shown. The region of parameter space excluded by the $w_0 + w_1 \leq 0$ prior is filled with upwards-sloping stripes.

IV. RESULTS AND DISCUSSION

A. Goals

As we have said, the most important question in the study of dark energy today is whether the dark energy is or is not a cosmological constant. If dark energy is shown not to be a cosmological constant, the next questions that arise are again qualitative: Is the equation of state greater or less than -1? Does it vary with time? The actual values of $w(0)$ and $w'(0)$ will become important only in the more distant future, when theoretical models for the form of $w(z)$ are available. Thus, we emphasize that our goal is to answer these qualitative questions in a careful, parametrization-independent way, rather than to find specific values for $w(0)$ and $w'(0)$ within a particular parametrization.

B. Analysis of current data

Keeping these goals in mind, we used χ^2 minimization to analyze current data from the CMB power spectrum [9], the SN Ia "gold set" [8], and the galaxy power spectrum [12]. We began by using (4) to parametrize the dark energy equation of state. The contours obtained are plotted in Fig. 6, with grid spacings $\Delta_{w_0} = 0.06$ and $\Delta_{w_1} = 0.15$. The resulting 1σ and 2σ constraints on the dark energy parameters are $w_0 = -1.38^{+0.08+0.30}_{-0.20-0.55}$ and $w_1 = 1.2^{+0.40+0.64}_{-0.16-1.06}$, with a best-fit χ^2 value of 1611. Since 1σ contours are not useful for ruling out models, we selected our grid spacings so as to obtain precise 2σ constraints. Thus, we consider our 2σ contours to be more reliable than our 1σ contours, in Fig. 6 as well as in subsequent contour plots.

ΛCDM models are not conclusively ruled out by our results. Compared to the best-fit model in Fig. 6, the ΛCDM model has a χ^2 value that is higher by 5. However, the cosmological constant is a "simpler" model of dark energy than the $w(z)$ parametrizations considered here, in the sense that the ΛCDM model has two fewer variable parameters than (1), (2), and (4). Thus the ΛCDM model has $\chi^2/\text{d.o.f.} = 1616/1514 = 1.0676$, while the best-fit model from Fig. 6 has $\chi^2/\text{d.o.f.} = 1611/1512 = 1.0656$. In the approximation that uncertainties in the data points are Gaussian, these correspond to probabilities of $P_{\Lambda\text{CDM}} = 0.0336$ and $P_{\text{best-fit}} = 0.0378$. For comparison, a point on the edge of the 2σ contour in Fig. 6 has $\chi^2/\text{d.o.f.} = 1615/1512 = 1.0682$ and probability 0.0324. In this sense, the ΛCDM model is more probable than some points within the 2σ contour. Although the data favor $w_0 < -1$ and $w_1 > 0$, the cosmological constant is not decisively ruled out as a model of dark energy.

Moreover, we have not considered systematic uncertainties in the supernova data, which can degrade constraints on the equation of state. As an optimistic estimate of the effects that such a systematic will have on dark energy constraints, we assumed an uncorrelated systematic uncertainty $\delta m = 0.04$, in redshift bins $\Delta z = 0.1$, and reanalyzed the data. The added uncertainty caused the 2σ contour to broaden to include the cosmological constant, while the best-fit model remained the same.

It is troubling that the best-fit model in Fig. 6 is so close to the boundary $w_0 + w_1 = 0$ of the dark energy parameter space. This is despite the fact that (4), out of the three 2-parameter equations of state illustrated in Fig. 1, covers the greatest range of parameters in the $(z, w(z))$ plane. Parametrization (2), widely used in the literature, is more restrictive than (4), and therefore should have more problems with this boundary. We repeated our analysis using (2), obtaining the χ^2 contours shown in Fig. 7 with grid spacings $\Delta_{w_0} = 0.1$ and $\Delta_{w_a} = 0.25$. The resulting 2σ bounds are $w_0 = -1.3^{+0.39}_{-0.34}$ and $w_a = 1.25^{+0.40}_{-2.17}$, with a best-fit χ^2 value of 1613. Thus we see that the allowed region shifts significantly when we switch to parametrization (2), with $w'(0) < 0$ models falling within the 2σ contours. Also, the minimum χ^2 value goes up by 1.8.

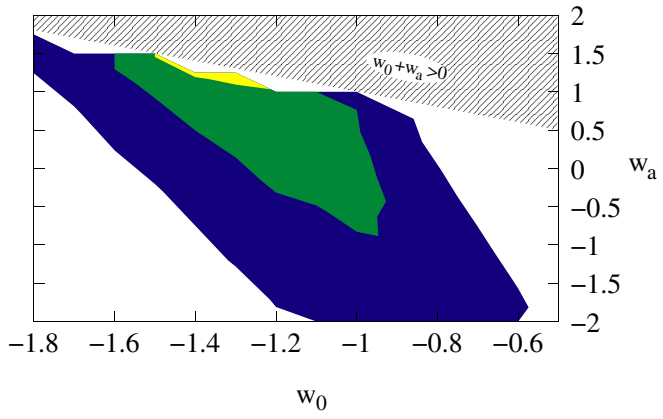

FIG. 7 (color online). Same as Fig. 6, except that the dark energy parametrization (2) has been used. The region of parameter space excluded by the $w_0 + w_a \leq 0$ prior is filled with upwards-sloping stripes.

These shifts are better understood when the χ^2 functions corresponding to the two parametrizations are plotted together in the $(w_0, \bar{w}')$ plane [with $\bar{w}' \equiv w(1) - w(0)$], as in Fig. 8. Note that the two sets of χ^2 contours would be nearly identical if the region of parameter space between the dotted lines were removed. This region corresponds to the slice of the $(z, w(z))$ plane between the dashed and solid lines in Fig. 1, which is allowed by parametrization (4) but not by (2). Thus, the difference between the constraints found using (2) and (4) is directly related to the parametrization, and particularly, to the high redshift $w(z)$ constraint discussed in Sec. II A. Evidently, switching parametrizations from (4) to (2) moves the boundary downwards, pushing the contours in the direction of decreasing $\bar{w}'$. Since the contours in Fig. 6 are still near the boundary, a parametrization that allows larger values of $\bar{w}'$ may allow the contours to shift even more in that direction. It is possible that such a parametrization would favor $w_0 < -1$ and $\bar{w}' > 0$ to an even larger degree, leaving the ΛCDM model less favored.

Comparison with the published literature shows that our results are consistent with others obtained using various combinations of cosmological probes. Table III lists sev-

TABLE III. Dynamical dark energy constraints from current data. The vanilla parameter space is spanned by the six parameters $(h, \omega_m, \omega_b, \tau, A, n_s)$. The cosmological probes used are *bias* = SDSS galaxy bias, *CMB* = WMAP CMB power spectra, *Ly-α* = SDSS Lyman-α, $P(k)$ = SDSS galaxy power spectrum, *SNIa* = SN Ia "gold set," and *X-ray* = Chandra X-ray clusters.

Reference	Probes included	Parameters varied	Priors	Dark energy constraints
[8]	*SN Ia*	w_0, w', Ω_m	$\Omega_m = 0.27 \pm 0.04$	$w_0 = -1.31^{+0.22}_{-0.28}$, $w' = 1.48^{+0.81}_{-0.90}$
[54]	*CMB*, *SN Ia*, $P(k)$, *bias*, *Ly-α*	"vanilla," w_0, w_a	$\tau < 0.3$	$w_0 = -0.981^{+0.193+0.384+0.568}_{-0.193-0.373-0.521}$, $w_a = -0.05^{+0.65+1.13+1.38}_{-0.83-1.92-2.88}$
[106]	*CMB*, *SN Ia*, $P(k)$	"vanilla," 4 $w(z)$ parameters	$h = 0.72 \pm 0.08$, $0 < \Omega_m < 1$, $0.014 < \omega_b < 0.04$, $0 < \tau < 1$, $0.6 < n_s < 1.4$	$w_0 = -1.43^{+0.16}_{-0.38}$, $\frac{dw}{dz}\|_{z=0} = 1.0^{+1.0}_{-0.8}$
[107]	*SN Ia*	w_0, w', Ω_m	$d_{AC}^{(\mathrm{dec})}\omega_m^{1/2}/c = 1.716 \pm 0.062$, $\frac{d\ln D}{d\ln a}\|_{z=0.15} = 0.51 \pm 0.11$	$-1.05 < w_0 < -0.29$, $-1.89 < w' < 0.05$ [a]
[107]	*SN Ia*	w_0, w', Ω_m	$\Omega_m = 0.27 \pm 0.04$	$-1.39 < w_0 < -0.25$, $-2.61 < w' < 1.49$ [a]
[108]	*SN Ia*	Ω_m, 3 $w(z)$ parameters	$d_{AC}^{(\mathrm{dec})}\omega_m^{1/2}/c = 1.710 \pm 0.137$, $\omega_b = 0.024$, $\omega_m = 0.14 \pm 0.02$	$\bar{w}\|_{0<z<0.414} = -1.287^{+0.016}_{-0.056}$, $\bar{w}\|_{0.414<z<1} = -0.229^{+0.070}_{-0.117}$, $\bar{w}\|_{1<z<1.755} = 0.142^{+0.051}_{-0.033}$
[109]	*SN Ia*	w_0, w_a	$\Omega_m = 0.27$	$w_0 = -1.38 \pm 0.21$, $w_a = 2.78 \pm 1.32$
[109]	*SN Ia*	w_0, w_a	$\Omega_m = 0.31$	$w_0 = -1.35 \pm 0.24$, $w_a = 2.32 \pm 1.56$
[109]	*SN Ia*	w_0, w_a	$\Omega_m = 0.35$	$w_0 = -1.3 \pm 0.29$, $w_a = 1.64 \pm 1.95$
[110]	*CMB*, *SN Ia*, *X-ray*	"vanilla," bias, w_0, w_a	bias $= 0.824 \pm 0.089$	$w_0 = -1.16^{+0.22}_{-0.19}$, $w_0 + w_a = -0.05^{+0.09}_{-1.17}$
[110]	*CMB*, *SN Ia*, *X-ray*	"vanilla," bias, Ω_K, w_0, w_a	bias $= 0.824 \pm 0.089$, $\tau < 0.3$	$w_0 = -1.14^{+0.31}_{-0.21}$, $w_0 + w_a = -0.09^{+0.12}_{-2.16}$
[110]	*CMB*, *SN Ia*, *X-ray*	"vanilla," bias, 3 $w(z)$ parameters	bias $= 0.824 \pm 0.089$	$w_0 = -1.23^{+0.34}_{-0.46}$, $\lim_{z\to\infty} w(z) = -0.12^{+0.11}_{-0.76}$
This work	*CMB*, *SN Ia*, $P(k)$	"vanilla," w_0, w_1	for priors see Table I	$w_0 = -1.38^{+0.30}_{-0.55}$, $w_1 = 1.20^{+0.64}_{-1.06}$ (2σ constraints)
This work	*CMB*, $P(k)$, *SN Ia* (syst. $\delta m = 0.04$)	"vanilla," w_0, w_1	for priors see Table I	$w_0 = -1.36^{+0.52}_{-0.56}$, $w_1 = 1.20^{+0.60}_{-1.88}$ (2σ constraints)
This work	*CMB*, *SN Ia*, $P(k)$	"vanilla," w_0, w_a	for priors see Table I	$w_0 = -1.3^{+0.39}_{-0.34}$, $w_a = 1.25^{+0.40}_{-2.17}$ (2σ constraints)

[a]Bounds taken from plot of 68% probability contour.

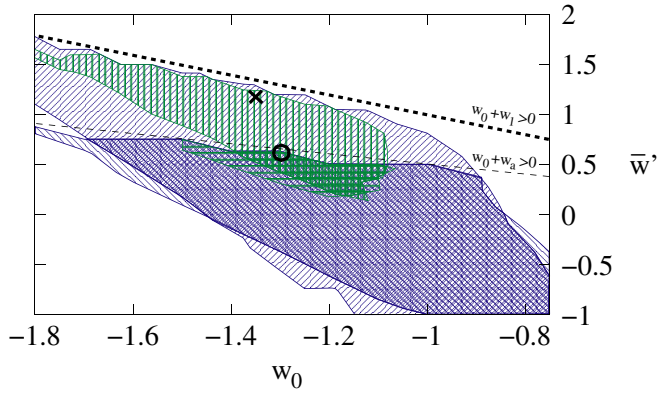

FIG. 8 (color online). Comparison of the two dark energy parametrizations (2) and (4). Contours corresponding to (4) are filled in with vertical stripes ($\chi^2 = 1615$ contour) or upwards-sloping stripes ($\chi^2 = 1620$ contour), and the best-fit model is marked by an "X." Contours corresponding to (2) are filled in with horizontal stripes ($\chi^2 = 1615$ contour) or downwards-sloping stripes ($\chi^2 = 1620$ contour), and the best-fit model is marked by an "O." Note that the $\chi^2 = 1615$ and $\chi^2 = 1620$ contours are the 2σ and 3σ contours, respectively, of parametrization (4). The thick and thin dashed lines correspond to the lines $w_0 + w_1 = 0$ and $w_0 + w_a = 0$, respectively.

eral recent analyses, along with the parameters and $w(z)$ parametrizations used [parameters w', w_a, and w_1 imply parametrizations (1), (2), and (4), respectively], the priors, and the resulting $w(z)$ constraints. When $w(z)$ constraints using the same equation of state parametrizations are compared, our results are consistent with those in Table III at the 2σ level. In addition, the results of [8,107], obtained using parametrization (1) and SN Ia data, are consistent with our constraints using either of the parametrizations (2) and (4). It is reassuring that our χ^2 minimization procedure, which handles parameter degeneracies differently than marginalization, obtains consistent results.

Several papers list constraints on $w(z)$ at specific values of z, as shown in Table IV. It is evident from the table that $w(0.3)$ is well constrained and parametrization independent. Our results for $w(0.3)$ are in excellent agreement with those of [54], even when their three-parameter equation of state (3) is used. Meanwhile, the equation of state at $z = 1$ is less well constrained, though once again our results agree with those of [54] at the 2σ level. Parametrization (4) evidently prefers higher values of $w(1)$ than does (2). One would expect the addition of the third parameter in (3) to bridge the gap between constraints using (2) and (4). However, not even (3) is able to reproduce the characteristics $w(0) \approx -1.4$, $w(0.3) \approx -1$, and $w(1) \approx -0.2$ of the best-fit models found using (4). Since our best w models are qualitatively different from those allowed using the parametrizations (2) and (3), there is still no discrepancy between our results and those of [54] for $w(1.0)$. Finally, recall that the two-parameter equations of state (1), (2), and (4) relate $w(z)$ and its derivative, at low redshifts, to the equation of state in the large redshift limit. Our constraints on the large redshift value of the equation of state, $\lim_{z\to\infty} w(z)$, agree closely with those of [110]. These results appear to be independent of parametrization; analyses with three different parametrizations agree that $w(z)$ at large redshifts is slightly less than zero.

TABLE IV. Constraints on $w(z)$ at several redshifts.

z	Reference	Parametrization	$w(z)$ constraint
0.3	[54]	(2)	$-1.011^{+0.176}_{-0.215}$ (95.5%)
	[54]	(3)	$-0.981^{+0.205}_{-0.249}$ (95.5%)
	This work	(4)	$-1.02^{+0.18}_{-0.33}$ (2σ)
	This work	(2)	$-1.01^{+0.19}_{-0.29}$ (2σ)
1	[54]	(2)	$-1.00^{+0.27}_{-0.66}$ (95.5%)
	[54]	(3)	$-1.03^{+0.39}_{-0.58}$ (95.5%)
	This work	(4)	$-0.18^{+0.12}_{-0.80}$ (2σ)
	This work	(2)	$-0.68^{+0.08}_{-0.74}$ (2σ)
∞	[110]	(2)	$-0.05^{+0.09}_{-1.17}$
	[110]	3 $w(z)$ parameters	$-0.12^{+0.11}_{-0.76}$
	This work	(4)	$-0.18^{+0.12}_{-0.80}$ (2σ)
	This work	(2)	$-0.05^{+0.05}_{-1.78}$ (2σ)

Our uncertainties in the dark energy parameters are mostly in agreement with similar analyses that include CMB and SN Ia data. Our 2σ uncertainties in w_0 and $w_0 + w_a = \lim_{z\to\infty} w(z)$ are approximately twice as large as the 68.3% constraints of [110], just as expected. Also, our 2σ constraints on w_0 are about twice as large as the 1σ uncertainties of [106]. Their looser bounds on $w'(0)$ can be attributed to the fact that they use a four-parameter equation of state, and marginalize over parameters other than those reported. Meanwhile, comparison of our results with [54] provides an example of parametrization effects on the dark energy constraints. Their 95.5% upper and lower bounds on w_0 are nearly the same as our 2σ bounds, and their 95.5% lower bound on w_a is somewhat tighter than ours. However, our upper bound on w_a is smaller than theirs by a factor of 3, due to the fact that our best-fit model is much nearer to the boundary $w_0 + w_a = 0$ of parameter space. Still, the boundary has some effect on their 95.5% and 99.86% probability bounds on w_a. Although their 68.32% upper and lower bounds are nearly the same, their 99.86% upper bound is smaller than the lower bound by a factor of 2. Thus, it would be interesting to see their analysis repeated with parametrizaton (4), which has a less restrictive boundary.

The effects of systematic uncertainties can be estimated by comparing the analysis procedures used by the studies listed in Table III, as well as the locations of the resulting contours in parameter space. Reference [54] finds 68% and 95% contours centered near the ΛCDM model, while [8,106,108–111] as well as our analysis find contours that lie mostly in the $w_0 < -1$, $w'(0) > 0$ region. Even when the analysis of [54] is repeated without the Lyman-α

and galaxy bias data sets, their preferred models are still close to the ΛCDM model [112]. Since both studies use the standard SN Ia likelihood, the difference between their result and ours must come from either their CMB likelihood function [113] or their galaxy power spectrum analysis [54,114]. Reference [113] claims that the WMAP likelihood approximation is inaccurate at low l, and that the WMAP foreground removal procedure may lead to a suppression of low-l power. Their likelihood function is designed to correct these problems. Meanwhile, their galaxy power spectrum analysis uses SDSS measurements up to $k = 0.2h/\mathrm{Mpc}$, a range which extends into the nonlinear regime. The combined effect of these two changes is to move the contours very close to the ΛCDM model, which is disfavored by $\Delta\chi^2 = 3$ in our analysis with the same $w(z)$ parametrization. Thus, differences in the CMB and galaxy power spectrum likelihood functions lead to a shift of over 1σ in the χ^2 contours.

We attempted to reproduce this shift by using only the multipoles $l \geq 20$ in our CMB analysis. If the low multipoles were responsible for the shift, then neglecting them would enlarge the χ^2 contours and move them towards the ΛCDM model. However, as shown in the third column of Table V, the allowed region actually moves away from that of [54], although it does broaden somewhat. Not only does this test fail to explain the difference between the regions of parameter space preferred by [54] and our results, it also demonstrates that the CMB analysis is sensitive to the low-l region of the power spectrum. Since there is an ongoing debate about the proper handling of the low multipoles [113], this sensitivity to that region of the power spectrum is worrisome.

Recall that switching dark energy parametrizations can change the uncertainties in $w(0)$ and $w'(0)$. In order to test the effects of this parametrization dependence in combination with the low-l sensitivity, we imposed the prior constraint $w_0 + 2w_1 = w_0 + 2\bar{w}' \geq 0$ on the analysis with CMB $l \geq 20$. This allowed us to estimate the constraint on w_a that we would have obtained if we had repeated the analysis with parametrization (2). The resulting 2σ constraints, shown in the fourth row of Table V, are very similar to those found by the standard analysis using parametrization (2). They have not moved appreciably towards the ΛCDM model, though the uncertainties have grown. The slight shift away from ΛCDM seen without the prior $w_0 + 2\bar{w}' \geq 0$ has been hidden by the imposition of that prior. This implies that the parametrization dependence of the results conceals some of their sensitivity to low-l CMB data. Once again, we are unable to reproduce the shift in the location of the equation of state contours. The explanation may have to do with the details of the CMB likelihood function used by [54], or with their galaxy power spectrum analysis. These differences between the likelihood functions should be examined critically.

Similarly, the SN Ia likelihood function used by [107] causes the dark energy constraints to shift relative to those in [8], even when the same $w(z)$ parametrizations and Ω_m priors are used. Reference [107] uses supernova flux averaging [115] to handle systematic effects due to the weak lensing of supernovae [116]. The flux averaging method assumes that uncertainties in SN Ia fluxes, rather than in magnitudes, are Gaussian. If uncertainties are actually Gaussian in magnitude, this introduces a bias [115]; conversely, if uncertainties are Gaussian in flux, then the standard SN Ia analysis is biased. The net effect of the flux averaged likelihood function is to weaken constraints on w_0 and w', and to shift them both by about 1σ towards the ΛCDM model.

Another SN Ia systematic effect, not included in any of the analyses in Table III, is the dimming of supernovae by astrophysical dust. Reference [117] considers several types of intergalactic dust, and constrains supernova dust dimming to be less than 0.2 magnitudes. The upper bound on dust dimming is not much less than the mean SN Ia magnitude uncertainty in the current data set, which suggests that dust dimming can cause a significant bias in dark energy constraints. Since the dimming of SNe Ia provides evidence for accelerating cosmological expansion, additional dimming due to dust will appear to exaggerate this acceleration, leading to an artificially low w.

To summarize, current data are not precise enough to address whether or not the dark energy is a cosmological constant. A careful study of the current data, and comparisons with other recent analyses, reveal several obstacles to a satisfactory understanding of the dark energy. The degeneracy between w_0 and w_1 remains unresolved, and the allowed 2σ ranges for w_0 and w_1 are at least $-1.93 < w_0 < -1.08$ and $0.14 < w_1 < 1.84$. Furthermore, this result is dependent on the parametrization chosen for the dark energy equation of state. In particular, problems arise

TABLE V. Consistency checks of our current $w(z)$ constraints. All constraints shown are at the 2σ level. The "standard" analyses below use WMAP, SDSS, and SN Ia gold set data, with priors as shown in Table I.

Analysis	Parametrization	w_0 (to 2σ)	w_1 or w_a (to 2σ)
Standard	(4)	$-1.38^{+0.30}_{-0.55}$	$w_1 = 1.2^{+0.64}_{-1.06}$
Standard	(2)	$-1.3^{+0.39}_{-0.34}$	$w_a = 1.25^{+0.40}_{-2.17}$
CMB $l \geq 20$	(4)	$-1.63^{+0.43}_{-0.65}$	$w_1 = 1.5^{+0.45}_{-1.67}$
$w_0 + 2w_1 \geq 0$, CMB $l \geq 20$	(4)	$-1.25^{+0.40}_{-0.38}$	$w_1 = 0.6^{+0.23}_{-1.4}$, $w_a \approx 2\bar{w}' = 1.2^{+0.46}_{-2.8}$

when the 1σ and 2σ contours lie near a boundary of the dark energy parameter space, as they do at present. More generally, uncertainties in the equation of state parameters depends on the location of the best-fit model in the parameter space. Aside from the parametrization-dependence issues, analyses that use the same data, but different treatments of the systematics, find best-fit models differing by $\sim 1\sigma$. The combination of parametrization-dependence and systematic effects is enough to shift the best-fit model by more than 2σ. Thus we cannot rule out the ΛCDM model at present.

C. Forecasts using simulated data

Next we ask, when data from future probes are available, how close can we come to achieving our goal of distinguishing between a cosmological constant and other forms of dark energy. The dark energy parameter space is continuous, with nonconstant $w(z)$ models arbitrarily close to the ΛCDM model. Unless we are lucky and find a dark energy significantly different from the cosmological constant, the best we can do is to distinguish between models separated by some minimum distance in parameter space.

Thus, we begin by identifying a set of reasonable milestones against which progress in $w(z)$ constraints may be measured. Since we do not know ahead of time which best-fit model will be found, we will say that an experiment can distinguish between two points A and B in parameter space if, regardless of the location of the best-fit model, the 2σ contour around that best-fit model excludes either A or B (or both).

Our first milestone is to distinguish between a cosmological constant and a "dark energy" whose equation of state at $z = 1$ is $w(1) = 0$. This goal is motivated by current observations, rather than by theoretical considerations; several of the analyses listed in Table III, including our own, favor $w \approx 0$ at redshifts of order unity. We can distinguish between these two types of dark energy by ruling out either $w(1) = -1$ (ΛCDM model) or $w(1) = 0$. In the worst case, the best-fit equation of state will have $w(1) = -0.5$, meaning that the 2σ uncertainty in $w(1)$ must be brought below 0.5 in order to rule out one of the two types of dark energy. Thus, the first milestone is to decrease the uncertainty in w at $z = 1$ to less than 0.5.

As our second milestone, we would like to distinguish between the ΛCDM model and tracker quintessence [118] or tracker supergravity [119] models with $w_0 \gtrsim -0.8$, $w_1 > 0$. These are interesting, partly because they represent a large class of well-established, theoretically motivated models, and also because they make definite predictions that are clearly distinct from the ΛCDM model in parameter space. It is not clear whether such models are ruled out by current data; our analyses exclude them to greater than 2σ, but they are within the 95% probability contour of [54]. In the future, we can compare an arbitrary best-fit model to ΛCDM and tracker models by comparing their values of $w(z_*)$, where z_* is the redshift at which the uncertainty in $w(z)$ is a minimum. The ΛCDM model predicts $w(z_*) = -1$, while trackers have $w(z_*) \gtrsim -0.8$. In the worst case, the future best-fit model will have $w(z_*) \approx -0.9$. Therefore, in order to reach the second milestone, we must reduce the 2σ uncertainty in $w(z_*)$ to about 0.1.

Finally, our third milestone is to distinguish between ΛCDM and quintessence models that are near to it. We do not have in mind any particular class of theoretical models, so "near" is not well defined. As a reasonable third milestone, we consider aiming to distinguish ΛCDM from models with either $|w_0 + 1| \gtrsim 0.05$ and $w_1 = 0$, or $w_0 = -1$ and $|w_1| \gtrsim 0.05$. For this we will need both $\Delta w_0(2\sigma) \lesssim 0.025$ and $\Delta w_1(2\sigma) \lesssim 0.025$, that is, $\sigma_{w_0} \sim \sigma_{w_1} \sim 0.01$. If the ΛCDM model were to be the preferred model even when the equation of state uncertainties were reduced to this level, then it would probably be time to abandon our hopes of using $w(z)$ to study the nature of dark energy.

Now that Sec. IV B has pointed out several pitfalls in the analyses of current data, we make the reasonably optimistic assumption that the likelihood functions associated with the CMB, SNe Ia, and cosmic shear will be well understood by the end of the decade. We assume that these new, accurate likelihood functions will give no less cosmological information than the likelihood functions discussed in Secs. III B, III C, and III D. This assumption is optimistic; the conservative CMB foreground removal procedure of [113], as well as the inclusion of SN Ia dust dimming effects, should increase uncertainties in the dark energy parameters. Moreover, for weak lensing, several systematic effects (e.g. intrinsic alignments of source galaxies, selection biases, and residuals from the point spread function correction) need to be better understood and tightly controlled in order for this probe to achieve its full potential [120].

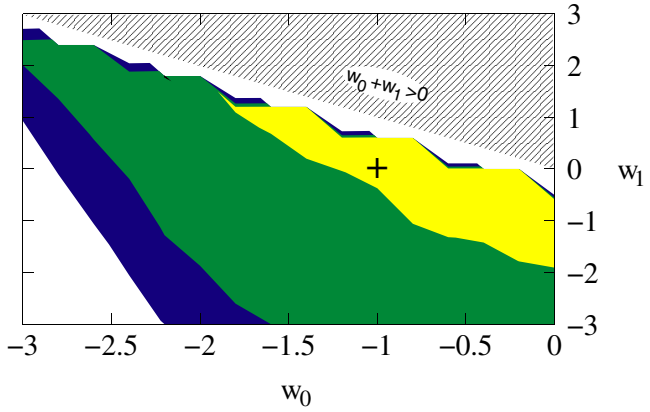

FIG. 9 (color online). Forecast CMB constraints on dark energy. The 1σ, 2σ, and 3σ contours are shown. The location of the fiducial model is marked by a "+" sign.

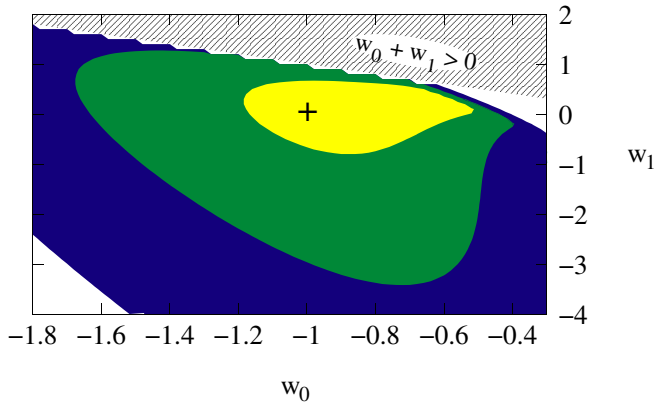

FIG. 10 (color online). SN Ia contours for the simulated data set shown in Fig. 3. The 1σ, 2σ, and 3σ contours are shown. The location of the fiducial model is marked by a "+" sign.

Also, our forecasts are based on a ΛCDM fiducial model, since $(w_0 = -1, w'(0) = 0)$ is far from both the parameter space boundaries $w_0 + w_1 = 0$ and $w_0 + w_a = 0$. From now on, we limit our study to the parametrization (4) alone. Assuming that our χ^2 contours stay away from the boundaries, we can compare constraints between parametrizations (2) and (4) using the "rule of thumb" $\sigma_{w_1} = \sigma_{\bar{w}'} \approx \sigma_{w_a}/2$, where the average low redshift derivative $\bar{w}' \equiv w(1) - w(0)$. The factor of 1/2 means that, even when parameter space boundaries are unimportant, the uncertainty in the derivative $w'(0)$ is parametrization dependent.

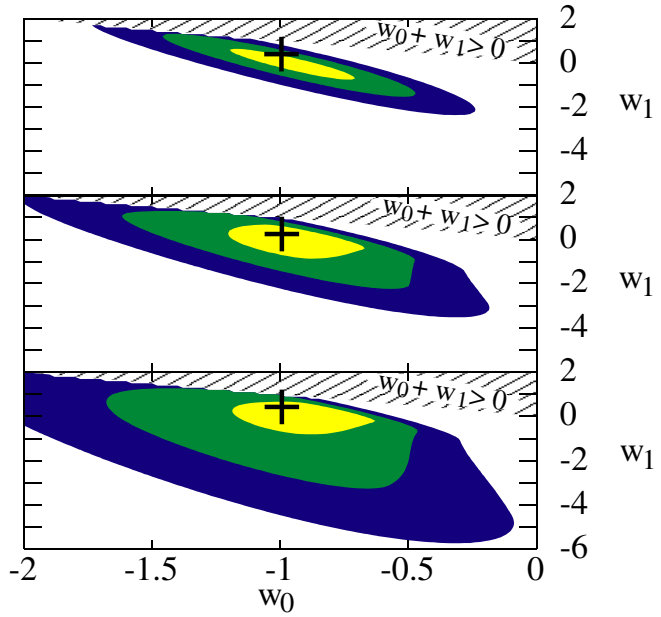

FIG. 11 (color online). SN Ia contours for the simulated data set shown in Fig. 3, assuming the prior constraints $\Omega_m = 0.31$ (top), $\Omega_m = 0.31 \pm 0.05$ (middle), and $\Omega_m = 0.31 \pm 0.10$ (bottom). The 1σ, 2σ, and 3σ contours are shown. The location of the fiducial model is marked by a "+" sign.

Dark energy constraints provided by eight years of simulated WMAP data alone are shown in Fig. 9, with grid spacings $\Delta_{w_0} = 0.3$ and $\Delta_{w_1} = 0.6$. Models in the upper right-hand section of Fig. 9 are ruled out by the prior constraint $w_0 + w_1 \leq 0$. Meanwhile, the requirement that $h < 1.1$ eliminates models in the lower left-hand corner of the plot. Therefore, to 2σ, virtually no constraints are imposed on w_0 and w_1 within the ranges shown in Fig. 9. Such weak CMB constraints on dynamical dark energy are to be expected, due to the angular diameter distance degeneracy.

Given the fairly weak priors used here, the supernovae alone were also unable to provide interesting constraints on dynamical dark energy. Analysis of the supernova data set shown in Fig. 3 gave deceptively tight constraints on w_1; see Fig. 10, with grid spacings $\Delta_{w_0} = 0.02$ and $\Delta_{w_1} = 0.1$. However, multiple Monte-Carlo simulations of SN Ia data sets yielded 2σ constraints that varied widely from simulation to simulation. Three out of our five simulations had 2σ contours extending into the $w_1 < -8$ range.

The problem, as pointed out in [121], is that the dark energy density $\rho_{\rm de}(z)$ exhibits qualitatively very different behaviors for $w_1 > 0$ and $w_1 < 0$. When $w_1 > 0$, $\rho_{\rm de}(z)$ can remain a nontrivial fraction of the total energy density of the Universe up to redshifts of order unity. When $w_1 < 0$, $\rho_{\rm de}(z)$ drops quickly with increasing redshift, so that the dark energy is important only in the very recent past. Distinguishing between different dark energy models is difficult when $\rho(z)$ is very small.

Adopting strong priors on Ω_m significantly reduces these non-Gaussianities, as shown in Fig. 11 (top). When we fix $\Omega_m = 0.31$ and repeat the analysis of five simulated data sets, we find mean 2σ uncertainties on w_0 and w_1 of $\Delta w_0(2\sigma) = 0.522$ and $\Delta w_1(2\sigma) = 1.63$. The standard deviations in $\Delta w_0(2\sigma)$ and $\Delta w_1(2\sigma)$ are 0.036 and 0.21, respectively. Thus when Ω_m is fixed, the uncertainties vary by only a few percent from one simulation to another.

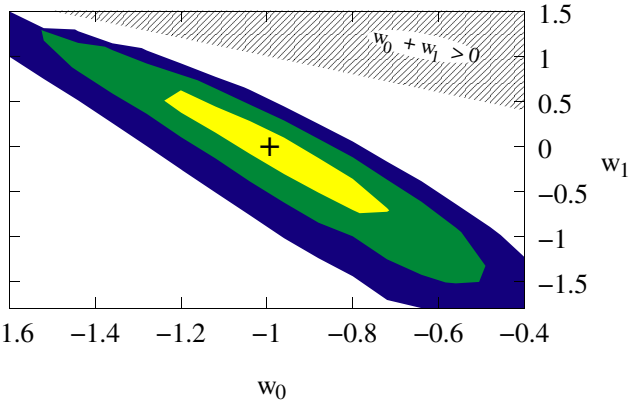

FIG. 12 (color online). Forecast CMB and SN Ia constraints on dark energy. The 1σ, 2σ, and 3σ contours are shown. The location of the fiducial model is marked by a "+" sign.

TABLE VI. Forecast 1σ constraints on the dark energy equation of state. [The vanilla parameter space is spanned by the six parameters $(h, \omega_m, \omega_b, \tau, A, n_s)$.]

Reference	Surveys included	Parameters varied; priors	Forecast constraints
[38]	Planck + WL (1000deg^2)	"vanilla," w_0, T/S; $w' = 0$	$\sigma_{w_0} = 0.15$
[39]	WL + COBE + photo z + Planck	ω_m, ω_b, n_s, m_ν, w_0; $w' = 0$, $\sigma_{\ln\omega_m} = .064$, $\sigma_{\ln\omega_b} = .035$, $\sigma_n = .04$, $\sigma_{m_\nu} = .58$	$\sigma_{w_0} = 0.19$
[40]	SNAP SNe Ia [syst. $\delta m = 0.0074(1+z)$]	w_0, w_a, Ω_m; $\sigma_{\Omega_m} = 0.03$, $\Omega_K = 0$	$\sigma_{w_0} = 0.09$, $\sigma_{\bar{w}'} = 0.31$
[40]	SNAP SNe Ia [syst. $\delta m = 0.0074(1+z)$]	w_0, w_a, Ω_m; Planck priors, $\Omega_K = 0$	$\sigma_{w_0} = 0.09$, $\sigma_{\bar{w}'} = 0.19$
[40]	SNAP SNe Ia [syst. $\delta m = 0.0074(1+z)$] +WL ($f_{\rm sky} = 0.025$)	w_0, w_a, Ω_m; $\Omega_K = 0$	$\sigma_{w_0} = 0.05$, $\sigma_{\bar{w}'} = 0.11$
[41]	Planck + WL ($f_{\rm sky} = 1$, tomography)	"vanilla," w_0, w_a, ω_ν, α_s, y_{He}	$\sigma_{w_0} = 0.056$, $\sigma_{w_a} = 0.087$
[41]	Planck + WL ($f_{\rm sky} = 0.5$, tomography)	"vanilla," w_0, w_a, ω_ν, α_s, y_{He}	$\sigma_{w_0} = 0.076$, $\sigma_{w_a} = 0.11$
[41]	4 yr. WMAP + WL ($f_{\rm sky} = 1$, tomography)	"vanilla," w_0, w_a, ω_ν, α_s, y_{He}	$\sigma_{w_0} = 0.064$, $\sigma_{w_a} = 0.11$
[42]	Planck + SNAP SNe Ia + WL ($f_{\rm sky} = 0.5$, tomography)	"vanilla," w_0, w_a, ω_ν, α_s, y_{He}	$\sigma_{w_0} = 0.05$, $\sigma_{w_a} = 0.1$
[43]	Planck + LSST cluster counts and power spectrum (200 000 clusters)	ω_b, ω_m, $\Omega_{\rm de}$, σ_8, n_s, w_0, w_a; linear biasing	$\sigma_{w_0} = 0.036$, $\sigma_{w_a} = 0.093$
[123]	1280 SNe [a]	w_0, w_a, Ω_m; Planck priors, $\sigma_{\Omega_m} = 0.03$, $\Omega_K = 0$	$\sigma_{w_0} = 0.27$, $\sigma_{\bar{w}'} = 0.57$
This work	8 yr. WMAP + ~2000 SNe (syst. $\delta m = 0.04$)	"vanilla," w_0, w_1; for priors see Table I	$\sigma_{w_0} = 0.26$, $\sigma_{w_1} = 0.82$
This work	8 yr. WMAP + ~2000 SNe (syst. $\delta m = 0.04$) +WL	"vanilla," w_0, w_1; for priors see Table I	$\sigma_{w_0} = 0.10$, $\sigma_{w_1} = 0.18$

[a]Irreducible magnitude systematic $\delta m^{\rm irr} = 0.01 + 0.06z$ for $z < 0.9$ or $0.1z$ for $z > 0.9$, extinction correction uncertainty $\delta m^{\rm ext} = 0.02$, low-mid z magnitude offset uncertainty $\delta m^{l-m,{\rm off}} = 0.02$, mid-high z magnitude offset uncertainty $\delta m^{m-h,{\rm off}} = 0.04$.

However, [122] points out the perils of assuming strong priors in the SN Ia analysis. Figures 11 (middle and bottom) show the effects of weakening the prior constraint on Ω_m to $\Omega_m = 0.31 \pm 0.05$ and $\Omega_m = 0.31 \pm 0.10$, respectively. Even with the relatively strong priors used in Fig. 11 (middle), constraints on the dark energy parameters are weakened, demonstrating the need to combine the supernovae with another data set.

Combination of the WMAP-8 and SN Ia data sets improved dark energy constraints considerably, as shown in Fig. 12, with grid spacings $\Delta_{w_0} = 0.08$ and $\Delta_{w_1} = 0.22$. As with the supernova analysis, five simulated data sets were analyzed separately in order to determine the dark energy constraints. We obtained the 2σ constraints $\Delta w_0(2\sigma) = 0.52$ and $\Delta w_1(2\sigma) = 1.65$. The standard deviations in the 2σ w_0 and w_1 uncertainties were 0.027 and 0.25, respectively. This implies that our forecast uncertainties are each correct to about 10%. We checked these constraints using a Fisher matrix calculation and found the 2σ constraints 0.44 and 1.46 in w_0 and w_1, respectively, consistent with our minimization results.

Our forecast uncertainty, in each of the equation of state parameters, is greater by a factor of 2–3 than that of [40] with SNe Ia and a prior on Ω_m, as shown in Table VI. Note that our 1σ uncertainties have been computed by dividing our 2σ uncertainties by two.

Next, the analysis was repeated with two different fiducial models, chosen to lie approximately along the line of degeneracy in the (w_0, w_1) plane. As shown in Fig. 13, the model $(w_0 = -1.3, w_1 = 0.5)$ had 2σ uncertainties of 0.73

TABLE VII. Consistency checks of our dark energy constraints. All constraints shown are at the 2σ level, with the standard deviations in constraints from multiple Monte-Carlo simulations shown when available. The standard analyses are those described in Secs. III B, III C, and III D while the other analyses differ from the standard ones as specified in the Analysis column.

Probes	Analysis	$\Delta w_0(2\sigma)$	$\Delta w_1(2\sigma)$
SN Ia	prior $\Omega_m = 0.31$	0.52 ± 0.036	1.63 ± 0.21
CMB + SN Ia	standard	0.52 ± 0.027	1.65 ± 0.25
	$f_{\rm sky}^2 \to f_{\rm sky}$ in (9)–(15)	0.52	1.31
	CMB $l \leq 400$	0.50	1.42
	1 yr. WMAP	0.47 ± 0.09	1.76 ± 0.42
	SN $\delta m = 0.06$	0.65	1.75
	SN $\delta m = 0.06z$	0.31	0.997
	SN $\delta m = 0$	0.19 ± 0.018	0.68 ± 0.071
CMB + SN Ia + WL	standard	0.20 ± 0.021	0.37 ± 0.034
	WL on linear scales only	0.39	0.96
	CMB $l \leq 400$	0.23	0.47
	SN $\delta m = 0.06$	0.24	0.48
	SN $\delta m = 0$	0.12 ± 0.007	0.29 ± 0.03

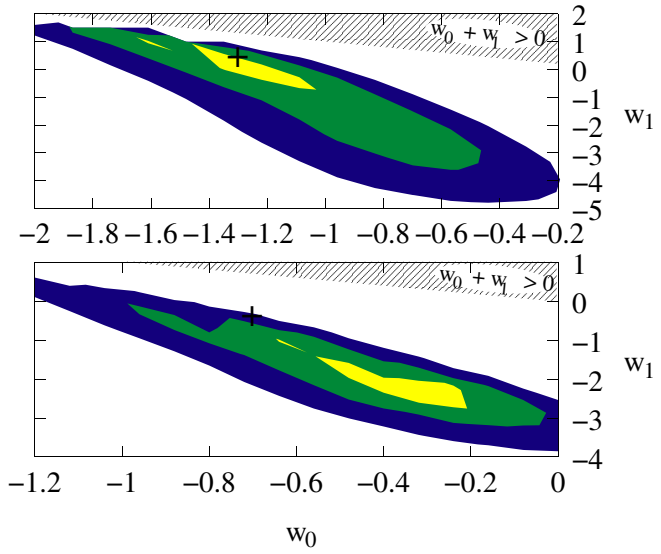

FIG. 13 (color online). χ^2 contours for CMB and SN Ia data simulated using the fiducial models ($w_0 = -1.3$, $w_1 = 0.5$) (top) and ($w_0 = -0.7$, $w_1 = -0.3$) (bottom). The 1σ, 2σ, and 3σ contours are shown. The location of the fiducial model is marked by a "+" sign.

and 2.58 on w_0 and w_1, respectively, which are significantly larger than those reported above. Meanwhile the model ($w_0 = -0.7$, $w_1 = -0.3$) had uncertainties of 0.48 and 1.58. These are consistent with our constraints obtained using the ΛCDM fiducial model.

Returning to our ΛCDM fiducial model, we repeated the analysis with different assumptions about the data in order to test the robustness of our forecast constraints. Table VII lists the new constraints obtained. The standard deviations in our original constraints are about 10%, so we did not consider a modification to be significant unless it changed constraints by at least 20%–30%. First we checked to what extent a CMB simulation without the extra factor of $f_{\rm sky}$ in the denominator of the covariance matrix (9)–(15) would improve our constraints. The difference turns out to be negligible. In fact, the final constraints are relatively independent of the details of the CMB simulation and analysis. Cutting off the CMB power spectrum at a maximum multipole of 400, or replacing the WMAP 8 year data set with a simulated 1 year data set, lead to insignificant changes in the dark energy constraints. On the other hand, the constraints are very sensitive to changes in the quality of the supernova data. Changing the SN Ia systematic uncertainty, or its redshift dependence, leads to significant changes in the dark energy constraints. Meanwhile, the final 2σ uncertainties provided by the combination of CMB and SN Ia data are nearly identical to those found by fixing Ω_m in the SN analysis alone. Thus, in some sense, adding the CMB data set is equivalent to fixing Ω_m as a function of w_0 and w_1 in the supernova analysis.

We began Sec. IV C by identifying three milestones for comparing constraints on w_0 and w_1. Recall that the first milestone is to distinguish between a cosmological constant and a dark energy with $w(1) = 0$. From our forecasts we find $\Delta w(1)(2\sigma) = 1.11$, which is more than twice as high as the uncertainty of 0.5 needed to distinguish between the two dark energy models. The second milestone, to distinguish between ΛCDM and tracker models of dark energy, is also not yet reached by the combination of CMB and SN Ia data sets. We find $\Delta w(z_*)(2\sigma) = 0.19$ at $z_* = 0.27$, twice the uncertainty of 0.1 needed to reach this milestone. We can see from Fig. 12 that, if we shifted the contours to be centered on ($w_0 = -0.9$, $w_1 = 0$), then the cosmological constant model as well as some of the tracker models ($w_0 \geq -0.8$, $w_1 > 0$) would be within the 2σ

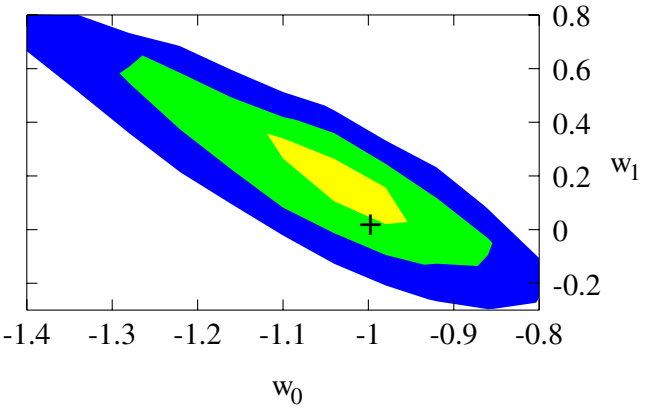

FIG. 14 (color online). Forecast CMB, SN Ia, and WL constraints on dark energy. The 1σ, 2σ, and 3σ contours are shown. The location of the fiducial model is marked by a "+" sign.

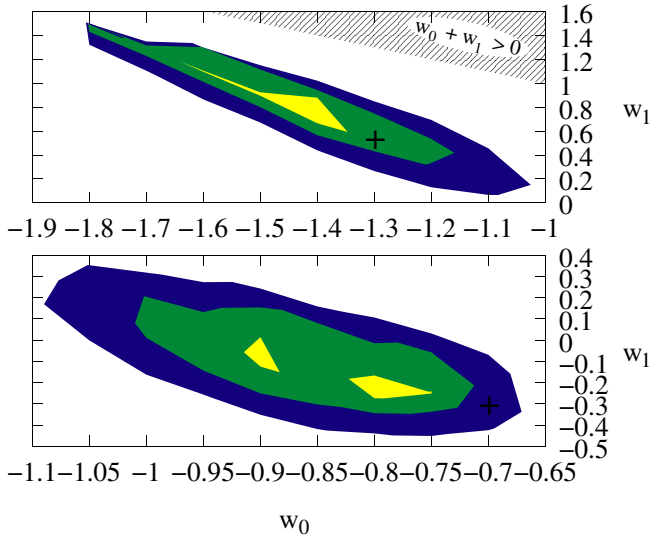

FIG. 15 (color online). χ^2 contours for CMB, SN Ia, and WL data simulated using the fiducial models ($w_0 = -1.3$, $w_1 = 0.5$) (top) and ($w_0 = -0.7$, $w_1 = -0.3$) (bottom). The 1σ, 2σ, and 3σ contours are shown. The location of the fiducial model is marked by a "+" sign.

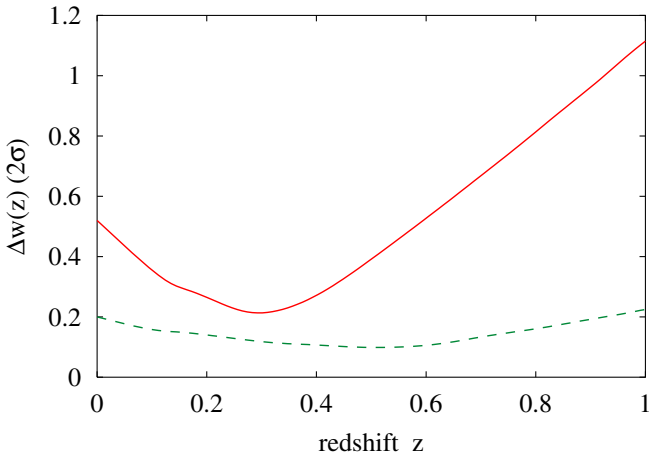

FIG. 16 (color online). $\Delta w(z)(2\sigma)$ as a function of z, for the data combinations CMB + SN Ia (upper, solid line) and CMB + SN Ia + WL (lower, dashed line).

contours. Thus we cannot confidently claim that the combination of CMB and SN Ia data can rule out either the ΛCDM model or the trackers. Finally, this combination is far from reaching the third milestone, which would require that the uncertainties in w_0 and w_1 be reduced by over an order of magnitude.

The addition of weak lensing to the analysis resulted in the contours shown in Fig. 14, with grid spacings $\Delta_{w_0} = 0.06$ and $\Delta_{w_1} = 0.12$. Weak lensing tightened the 2σ constraints to $\Delta w_0(2\sigma) = 0.20$ and $\Delta w_1(2\sigma) = 0.37$. The standard deviations in the 2σ uncertainties, found from five separate simulations, were 0.021 and 0.034 in $\Delta w_0(2\sigma)$ and $\Delta w_1(2\sigma)$, respectively. As above, the standard deviations in each of the w_0 and w_1 uncertainties were about 10%. We checked our results using a Fisher matrix calculation and found the 2σ constraints 0.16 and 0.38 in w_0 and w_1, respectively, consistent with our minimization results. Our constraints are about the same as those forecast for Supernova/Acceleration Probe (SNAP) SNe Ia with Planck priors, but worse by a factor of 2 than SNAP SNe Ia with weak lensing, as listed in Table VI. Galaxy cluster measurements based on the more ambitious Large Synoptic Survey Telescope (LSST) survey claim an improvement by a factor of 3 over our forecast w_0 constraints [43].

The analysis was repeated with two different fiducial models in order to assess the dependence of dark energy constraints on the fiducial model, as shown in Fig. 15. Moving from the ΛCDM fiducial to the fiducial model ($w_0 = -1.3, w_1 = 0.5$) increases uncertainties in w_0 and w_1 by about 70% each, to 0.34 and 0.63, respectively. Moving in the other direction along the degeneracy curve, to the fiducial model ($w_0 = -0.7, w_1 = -0.3$), leads to a modest decrease in w_0 and w_1 uncertainties to 0.15 and 0.28, respectively. Qualitatively, this is the same behavior as was seen with the CMB and SN Ia data combination.

Further tests of the robustness of our constraints revealed that, once again, CMB data at $l > 400$ do not contribute much to the dark energy constraints (see Table VII). Meanwhile, if the weak lensing analysis is restricted to linear scales, then constraints on w_0 and w_1 weaken considerably, as shown in Table VII. This is consistent with the findings of [39].

Comparing 2σ constraints with and without weak lensing (including nonlinear scales), we see that the uncertainties in w_0 shrink by a factor of 2.5, and the uncertainties on w_1 shrink by a factor of 4.5. In order to understand the contribution of weak lensing to the overall analysis, we compared $w(z)$ uncertainties as functions of redshift for the combinations CMB + SN Ia and CMB + SN Ia + WL, as shown in Fig. 16. Without weak lensing, $w(z)$ is well constrained only around $z \approx 0.3$. Evidently, weak lensing adds information on w at some higher redshift, complementing the constraints from CMB and SN Ia. The result is a $w(z)$ uncertainty that is not only lower, but much more uniform across the redshift range.

This improvement allows the combination of CMB, SN Ia, and WL data to reach two of the three milestones identified at the beginning of this section. At $z = 1$ we find $\Delta w(1)(2\sigma) = 0.22$, which will easily allow us to distinguish between a cosmological constant and dark energy models with $w(1) \approx 0$. Thus, weak lensing will either confirm or conclusively rule out the dark energies with $w_0 + w_1 \lesssim 0$ favored by our analysis of current data. Second, the constraint $\Delta w(z_*)(2\sigma) = 0.097$ at $z_* = 0.52$ is tight enough that this combination of data can distinguish between the cosmological constant and tracker models of dark energy. Thus, weak lensing will allow us to rule out a portion of the most interesting region of parameter space. On the other hand, our forecast dark energy constraints do not reach the third milestone, which calls for these 2σ uncertainties to be reduced to $\sim$0.025. In particular, the uncertainty in w_1 is higher than this by over an order of magnitude.

We have not included in our analysis either weak lensing tomography or galaxy cluster measurements, which may lower statistical uncertainties even further [43,124]. These have been analyzed by others and look promising. They suggest that we can approach the third milestone, but there is no method suggested so far for pushing substantially beyond their forecast constraints.

Moreover, we remind the reader that the constraints discussed above, as well as the improvement due to weak lensing, are based on several optimistic assumptions listed at the beginning of Sec. IV C. Systematic effects can increase uncertainties in w_0 and w_1. Also, if the best-fit dark energy model is near the boundary of the (w_0, w_1) parameter space, then $w(z)$ parametrization dependence will further weaken our constraints on the dark energy

parameters. In the worst-case scenario $w_0 + w_1 \approx 0$, the best-fit model will be near the boundary of parameter space; parametrization-related uncertainties in w_0 and $w'(0)$ could completely swamp any improvements.

V. CONCLUSIONS

The purpose of this investigation has been to determine how well $w(z)$ can be resolved using currently planned astronomical observations. The well-known challenge is that individual measurements do not constrain $w(z)$ directly, but rather some functional that depends on $w(z)$, integrals of $w(z)$, and a large set of additional parameters.

We have shown that the uncertainties in measuring w and dw/dz at $z = 0$ can be reduced dramatically by the beginning of the next decade, using a combination of the highest-quality CMB, SN, and WL data. However, the remaining uncertainties, $\Delta w_0(2\sigma) = 0.20$ and $\Delta w_1(2\sigma) = 0.37$, will not be enough to determine definitively whether dark energy is inert (a cosmological constant) or dynamical (quintessence), unless the true value of w differs from -1 by significantly more than 0.1. Unfortunately, many quintessence models have $|w_0 + 1| < 0.1$ and $|w_1| < 0.1$.

Our numerical studies illustrate how the measurements combine to produce this constraint. Even the best supernova measurements are degenerate under certain combinations of variations in $w(0)$, $w'(0)$, and Ω_m [37]. CMB constraints are degenerate along a surface in the space spanned by $w(0)$, $w'(0)$, h, and Ω_m. However, we have found (Fig. 12) that combining CMB and SN measurements effectively collapses the degeneracy in the Ω_m direction, leaving only the degeneracy in the $w(0)$, $w'(0)$ plane. We have shown that the CMB contribution to this degeneracy breaking comes entirely from the $l \leq 400$ region of the power spectrum. Since even the first year of WMAP data has reduced uncertainties in this range to near the cosmic variance level, we do not expect a significant improvement in dark energy constraints from further WMAP or Planck CMB data. Of course, this relies on our choice and number of cosmological parameters, and, in particular, our assumption that $\Omega_K = 0$. If curvature were considered, the angular diameter distance degeneracy would degrade the information on Ω_m provided by the first CMB acoustic peak, and better information on subsequent peaks could prove valuable. Also, we have not considered nonlinear effects such as the gravitational lensing of the CMB power spectra [125], which could provide valuable information on structure formation.

Meanwhile, the final constraints are sensitive to the supernova systematic uncertainties. A 50% increase in δm, from 0.04 to 0.06, changes the 2σ constraints on $w(0)$ by about 25%. After the CMB and SN data sets are combined, the remaining degeneracy runs along curves of $w(z)$ which intersect one another near $z = 0.3$. The uncertainty in $w(0.3)$ is roughly 0.2 at the 2σ level, depending on what functional forms for $w(z)$ are considered.

To break the degeneracy between $w(0)$ and $w'(0)$, more data must be co-added that can constrain $w(z)$ at a greater redshift. We have studied the weak lensing power spectrum as a means of breaking the $w(0)$-$w'(0)$ degeneracy. Our previous conclusion about the highest CMB multipoles remains valid; CMB data at $l > 400$ do not contribute to dark energy constraints even when weak lensing is considered. Furthermore, any improvements due to weak lensing depend crucially on our ability to use shear measurements on nonlinear scales. This will require a better understanding of systematics, such as intrinsic alignments of galaxies, as well as more accurate computations of the matter power spectrum on nonlinear scales in dynamical dark energy cosmologies. When CMB, SN, and WL are combined, the supernovae constrain $w(z)$ at low redshifts $z \approx 0.3$, while weak lensing constrains $w(z)$ at higher redshifts (see Fig. 16), leading to improvements of a factor of 2.5 in w_0 and a factor of 4.5 in w_1.

Section IV C began by identifying three milestones by which progress in dark energy constraints could be measured.

(i) Distinguish between $w(1) = -1$ and $w(1) \approx 0$. CMB and SN alone are unable to reach this milestone, while the combination of CMB, SN, and WL data can distinguish between these equations of state at the 4.5σ level.

(ii) Distinguish between $w = -1$ and tracker models with $w_0 \geq -0.8$, $dw/dz > 0$. Once again, CMB and SN alone are unable to reach this milestone. With WL added, Λ and trackers can be distinguished at the 2σ level.

(iii) Reduce 2σ uncertainties in w and dw/dz to ≈ 0.025. Even with CMB, SN, and WL data, this milestone remains unreached.

Thus the combination of CMB, SN Ia, and weak lensing is a promising tool for improving dark energy constraints. However, in the worst-case scenario that experiments find $w \approx -1$, these three probes cannot decisively rule out quintessence models in which w differs from -1 by a few percent.

Other works have considered highly ambitious surveys of the cluster abundance evolution [43], assuming large numbers of observed clusters, or of weak lensing tomography [124], based on multiple redshift bins and observations of large fractions of the sky. Both probes measure the structure growth rate as a function of redshift. These have the potential to improve statistical uncertainties significantly, by factors of 3–5 compared with our results, but concerns remain about systematic uncertainties [43,124]. Even taking the current estimated errors, uncertainties in w_0 and w_1 are several percent, which still allows a range of plausible quintessence models. Thus, unless we are lucky enough to find a dark energy that is very different from the cosmological constant, new kinds of measurements or an

experiment more sophisticated than those yet conceived will be needed in order to settle the dark energy issue.

ACKNOWLEDGMENTS

We thank N. Bahcall, R. Brustein, J. Gunn, C. Hirata, S. Ho, E. Linder, A. Makarov, I. Maor, J. Ostriker, A. Riess, U. Seljak, D. Spergel, C. Stubbs, Y. Wang, and D. Wesley for useful conversations. Our analysis was run on a Beowulf cluster at Princeton University, supported in part by NSF Grant No. AST-0216105. A. U. acknowledges the support of the National Science Foundation. M. I. acknowledges the support of the Natural Sciences and Engineering Research Council of Canada. This work was supported in part by US Department of Energy Grant No. DE-FG02-91ER40671 (PJS).

[1] A. G. Riess *et al.*, Astron. J. **116**, 1009 (1998).
[2] S. Perlmutter *et al.*, Astrophys. J. **517**, 565 (1999).
[3] A. G. Riess *et al.*, Astrophys. J. **536**, 62 (2000).
[4] A. G. Riess *et al.*, Astrophys. J. **560**, 49 (2001).
[5] J. L. Tonry *et al.*, Astrophys. J. **594**, 1 (2003).
[6] R. A. Knop *et al.*, Astrophys. J. **598**, 102 (2003).
[7] B. J. Barris *et al.*, Astrophys. J. **602**, 571 (2004).
[8] A. G. Riess *et al.*, Astrophys. J. **607**, 665 (2004).
[9] C. L. Bennett *et al.*, Astrophys. J. Suppl. Ser. **148**, 1 (2003).
[10] D. N. Spergel *et al.*, Astrophys. J. Suppl. Ser. **148**, 175 (2003).
[11] W. L. Freedman, *et al.*, Astrophys. J. **553**, 47 (2001).
[12] M. Tegmark *et al.*, Astrophys. J. **606**, 702 (2004).
[13] M. Tegmark *et al.*, Phys. Rev. D **69**, 103501 (2004).
[14] P. Fosalba, E. Gaztanaga, and F. Castander, Astrophys. J. **597**, L89 (2003).
[15] P. Fosalba and E Gaztanaga, Mon. Not. R. Astron. Soc. **350**, L37 (2004).
[16] R. Scranton *et al.*, astro-ph/0307335.
[17] N. Afshordi, Y.-S. Loh, and M. A. Strauss, Phys. Rev. D **69**, 083524 (2004).
[18] S. Boughn and R. Crittenden, Nature (London) **427**, 45 (2004).
[19] N. Padmanabhan *et al.*, astro-ph/0410360 [Phys. Rev. D (to be published)].
[20] P. J. E. Peebles and B. Ratra, Astrophys. J. Lett. **325**, L17 (1988).
[21] B. Ratra and P. J. E. Peebles, Phys. Rev. D **37**, 3406 (1988).
[22] I. Zlatev, L. Wang, and P. J. Steinhardt, Phys. Rev. Lett. **82**, 896 (1999).
[23] P. J. Steinhardt, L. Wang, and I. Zlatev, Phys. Rev. D **59**, 123504 (1999).
[24] R. R. Caldwell, Phys. Lett. B **545**, 23 (2002).
[25] S. M. Carroll, M. Hoffman, and M. Trodden, Phys. Rev. D **68**, 023509 (2003).
[26] V. K. Onemli and R. P. Woodard, Classical Quantum Gravity **19**, 4607 (2002).
[27] V. K. Onemli and R. P. Woodard, Phys. Rev. D **70**, 107301 (2004).
[28] T. Brunier, V. K. Onemli, and R. P. Woodard, Classical Quantum Gravity **22**, 59 (2005).
[29] M. Doran and J. Jäckel, Phys. Rev. D **66**, 043519 (2002).
[30] S. DeDeo, astro-ph/0411283.
[31] J. R. Bond, *et al.*, Phys. Rev. Lett. **72**, 13 (1994).
[32] J. R. Bond, G. Efstathiou, and M. Tegmark, Mon. Not. R. Astron. Soc. **291**, L33 (1997).
[33] M. Zaldarriaga, D. Spergel, and U. Seljak, Astrophys. J. **488**, 1 (1997).
[34] M. White, Astrophys. J. **506**, 495 (1998).
[35] G. Huey *et al.*, Phys. Rev. D **59**, 063005 (1999).
[36] G. Efstathiou and J. R. Bond, Mon. Not. R. Astron. Soc. **304**, 75 (1999).
[37] I. Maor, R. Brustein, and P. J. Steinhardt, Phys. Rev. Lett. **86**, 6 (2001).
[38] W. Hu, Phys. Rev. D **65**, 023003 (2002).
[39] D. Huterer, Phys. Rev. D **65**, 063001 (2002).
[40] G. Aldering, *et al.*, astro-ph/0405232 (see also http://snap.lbl.gov).
[41] Y.-S. Song and L. Knox, Phys. Rev. D **70**, 063510 (2004).
[42] L. Knox, A. Albrecht, and Y. S. Song, astro-ph/0408141.
[43] S. Wang *et al.* Phys. Rev. D **70**, 123008 (2004).
[44] D. Huterer and M. S. Turner, Phys. Rev. D **64**, 123527 (2001).
[45] K. Benabed and L. Van Waerbeke, Phys. Rev. D **70**, 123515 (2004).
[46] K. Abazajian and S. Dodelson, Phys. Rev. Lett. **91**, 041301 (2003).
[47] A. Refregier *et al.* Astron. J. **127**, 3102 (2004).
[48] A. Heavens, Mon. Not. R. Astron. Soc. **343**, 1327 (2003).
[49] P. Simon, L. J. King, and P. Schneider, astro-ph/0309032 [Astron. Astrophys. (to be published)].
[50] B. Jain and A. Taylor, Phys. Rev. Lett. **91**, 141302 (2003).
[51] G. M. Bernstein and B. Jain, Astrophys. J. **600**, 17 (2004).
[52] W. Jang *et al.*, in *Third Statistical Challenges in Modern Astronomy Conference, 2003* (Springer, New York, 2003), pp. 221–241.
[53] B. A. Bassett, P. S. Corasaniti, and M. Kunz, Astrophys. J. Lett. **617**, 1 (2004).
[54] U. Seljak *et al.*, Phys. Rev. D **71**, 103515 (2005).
[55] R. R. Caldwell *et al.*, Astrophys. J. **591**, L75 (2003).
[56] R. R. Caldwell and M. Doran, Phys. Rev. D **69**, 103517 (2004).
[57] M. Chevallier, D. Polarski, and A. Starobinsky, Int. J. Mod. Phys. D **10**, 213 (2001).
[58] E. V. Linder, Phys. Rev. Lett. **90**, 091301 (2003).

[59] M. Ishak *et al.*, Phys. Rev. D **69**, 083514 (2004).
[60] I. Tereno *et al.*, astro-ph/0404317.
[61] M. Ishak and C. Hirata, Phys. Rev. D **71**, 023002 (2005).
[62] W. H. Press, S. A. Teukolsky, W. T. Vetterling, and B. P. Flannery, *Numerical Recipes in C: The Art of Scientific Computing* (Cambridge University Press, Cambridge, England, 1992).
[63] M. M. Phillips, Astrophys. J. Lett. **413**, L105 (1993).
[64] M. Hamuy *et al.*, Bull. Am. Astron. Soc. **26**, 1362 (1994).
[65] A. G. Riess, W. H. Press, and R. P. Kirshner, Astrophys. J. **438**, L17 (1995).
[66] A. G. Riess, W. H. Press, and R. P. Kirshner, Astrophys. J. **473**, 88 (1996).
[67] S. Perlmutter *et al.*, Astrophys. J. **483**, 565 (1997).
[68] U. Seljak and M. Zaldarriaga, Astrophys. J. **469**, 437 (1996).
[69] R. Caldwell (private communication).
[70] L. Verde *et al.*, Astrophys. J. Suppl. Ser. **148**, 195 (2003).
[71] G. Hinshaw *et al.*, Astrophys. J. Suppl. Ser. **148**, 63 (2003).
[72] A. Kogut *et al.*, Astrophys. J. Suppl. Ser. **148**, 161 (2003).
[73] http://www.hep.upenn.edu/ max/sdsspars.html.
[74] W. L. Freedman, astro-ph/0411176.
[75] http://home.fnal.gov/ annis/astrophys/deCam/PAC04/proposal/DES_PAC_proposal_031104.pdf (see also http://home.fnal.gov/annis/astrophys/deCam).
[76] R. C. Smith *et al.*, Bull. Am. Astron. Soc. **34**, 1232 (2002).
[77] P. M. Garnavich *et al.*, Bull. Am. Astron. Soc. **34**, 1233 (2002).
[78] R. P. Kirshner *et al.*, in *Proceedings of the American Astronomical Society Meeting 202, #23.08, 2003*, (see also http://www.ctio.noao.edu/wsne).
[79] L.-G. Strolger *et al.*, *Proceedings of the American Astronomical Society Meeting 202, #25.05, 2003.*
[80] http://www-int.stsci.edu/strolger.
[81] D. S. Madgwick *et al.*, Astrophys. J. **599**, L33 (2003).
[82] W. M. Wood-Vasey *et al.*, New Astron. Rev. **48**, 637 (2004).
[83] http://cfht.hawaii.edu/SNLS (see also http://snls.in2p3.fr/conf/posters/AAS203/AAS04SNLS.v4.ppt for a recent poster).
[84] R. Pain *et al.*, Bull. Am. Astron. Soc. **34**, 1169 (2002).
[85] C. J. Pritchet, astro-ph/0406242.
[86] M. Sullivan, astro-ph/0410594.
[87] A. G. Kim *et al.*, Mon. Not. R. Astron. Soc. **347**, 909 (2004).
[88] C. Stubbs (private communication).
[89] J. R. Bond, A. H. Jaffe, and L. Knox, Astrophys. J. **533**, 19 (2000).
[90] Ya. B. Zeldovich and R. A. Sunyaev, Astrophys. Space Sci. **4**, 301 (1969).
[91] R. A. Sunyaev and Ya. B. Zeldovich, Comments Astrophys. Space Phys. **4**, 173 (1972).
[92] A. Blanchard and J. Schneider, Astron. Astrophys. **184**, 1 (1987).
[93] A. Kashlinsky, Astrophys. J. Lett. **331**, L1 (1988).
[94] K. M. Huffenberger, U. Seljak, and A. Makarov, Phys. Rev. D **70**, 063002 (2004).
[95] U. Seljak and C. M. Hirata, Phys. Rev. D **69**, 043005 (2004).
[96] C. M. Hirata, *et al.*, Phys. Rev. D **70**, 103501 (2004).
[97] C. R. Lawrence and A. E. Lange, Bull. Am. Astron. Soc. **29**, 1273 (1997).
[98] R. J. Laureijs, in *Proceedings of the International Astronomical Union Symposium No. 216, 2003.*
[99] N. Kaiser, Astrophys. J. **388**, 272 (1992).
[100] B. Jain and U. Seljak, Astrophys. J. **484**, 560 (1997).
[101] N. Kaiser, Astrophys. J. **498**, 26 (1998).
[102] J. M. Bardeen, J. R. Bond, N. Kaiser, and A. S. Szalay, Astrophys. J. **304**, 15 (1986).
[103] Chung-Pei Ma, R. R. Caldwell, Paul Bode, and Limin Wang, Astrophys. Lett. **521**, L1 (1999).
[104] R. E. Smith *et al.*, Mon. Not. R. Astron. Soc. **341**, 1311 (2003).
[105] http://pan-starrs.ifa.hawaii.edu/public/index.html.
[106] S. Hannestad and E. Mörtsell, J. Cosmol. Astropart. Phys. 09 (2004) 001.
[107] Y. Wang and M. Tegmark, Phys. Rev. Lett. **92**, 241302 (2004).
[108] U. Alam, V. Sahni, and A. A. Starobinsky, J. Cosmol. Astropart. Phys. 06 (2004) 008.
[109] T. R. Choudhury and T. Padmanabhan, Astron. Astrophys. **429**, 807 (2005).
[110] D. Rapetti, S. W. Allen, and J. Weller, Mon. Not. R. Astron. Soc. **360**, 555 (2005).
[111] P. S. Corasaniti *et al.*, Phys. Rev. D **70**, 083006 (2004).
[112] A. Makarov (private communication).
[113] A. Slosar, U. Seljak, and A. Makarov, Phys. Rev. D **69**, 123003 (2004).
[114] U. Seljak *et al.*, Phys. Rev. D **71**, 043511 (2005).
[115] Y. Wang, Astrophys. J. **531**, 676 (2000).
[116] Y. Wang, J. Cosmol. Astropart. Phys. 03 (2005) 005.
[117] L. Östman and E. Mörtsell, J. Cosmol. Astropart. Phys. 02 (2005) 005.
[118] I. Zlatev, L. Wang, and P. J. Steinhardt, Phys. Rev. Lett. **82**, 896 (1999).
[119] P. Brax and J. Martin, Phys. Lett. B **468**, 40 (1999).
[120] A. Refregier, Annu. Rev. Astron. Astrophys. **41**, 645 (2003).
[121] I. Maor *et al.*, Phys. Rev. D **65**, 123003 (2002).
[122] J.-M. Virey *et al.*, Phys. Rev. D **70**, 121301 (2004).
[123] E. V. Linder and R. Miquel, Phys. Rev. D **70**, 123516 (2004).
[124] M. Ishak, astro-ph/0501594 [Mon. Not. R. Astron. Soc. (to be published)].
[125] C. M. Hirata and U. Seljak, Phys. Rev. D **68**, 083002 (2003).